# A GRID NESTING METHOD FOR LARGE-EDDY SIMULATION OF PLANETARY BOUNDARY-LAYER FLOWS

PETER P. SULLIVAN[1], JAMES C. McWILLIAMS[1,2] and CHIN-HOH MOENG[1]
[1]*National Center for Atmospheric Research, P.O. Box 3000, Boulder, CO 80307-3000, U.S.A.;*
[2]*Department of Atmospheric Sciences, UCLA, Los Angeles, CA 90024, U.S.A.*

(Received in final form 5 April, 1996)

**Abstract.** A method for performing nested grid calculations with a large-eddy simulation code is described. A common numerical method is used for all meshes, and the grid architecture consists of a single outer or coarse grid, and nested or fine grids, which overlap in some common region. Inter-grid communication matches the velocity, pressure and potential temperature fields in the overlap region. Resolved and sub-grid scale (SGS) turbulent fluxes and kinetic energy on the fine grid are averaged to the coarse grid using a conservation rule equivalent to Germano's identity used to develop dynamic SGS models.

Simulations of a slightly convective, strong shear planetary boundary layer were carried out with varying surface-layer resolutions. Grid refinements in the $(x, y, z)$ directions of up to (5, 5, 2) times were employed. Two-way interaction solutions on the coarse and fine meshes are successfully matched in the overlap region on an instantaneous basis, and the turbulent motions on the fine grid blend smoothly into the coarse grid across the grid interface. With surface-layer grid nesting, significant increases in resolved eddy fluxes and variances are found. The energy-scale content of the vertical velocity, and hence vertical turbulent fluxes, appear to be most influenced by increased grid resolution. Vertical velocity spectra show that the dominant scale shifts towards higher wavenumbers (smaller scales) and the magnitude of the peak energy is increased by more than a factor of 3 with finer resolution. Outside of the nested region the average heat and momentum fluxes and spectra are slightly influenced by the fine resolution in the surface layer. From these results we conclude that fine resolution is required to resolve the details of the turbulent motions in the surface layer. At the same time, however, increased resolution in the surface layer does not appreciably alter the ensemble statistics of the resolved and SGS motions outside of the nested region.

## 1. Introduction

Although large-eddy simulation (LES) is a well established and powerful tool for the investigation of turbulent flows (Wyngaard, 1984; Reynolds, 1989), it is hindered by the enormous range of scales present in the planetary boundary layer (PBL). Simulations typically employ a single fixed grid or at most a stretched vertical grid (for a comparison of PBL codes see Nieuwstadt *et al.*, 1991 and Andrén *et al.*, 1994) which is only capable of resolving a limited range of scales; scales smaller than the grid mesh are delegated to sub-grid scale (SGS) motions, and are modeled using semi-empirical methods (e.g., Moeng, 1984; Sullivan *et al.*, 1994). Near boundaries this problem is exacerbated since the dominate energy containing scale is much smaller than the most energetic scales of the mid-PBL. Hence with a single fixed computational grid a large fraction of the eddy variances and fluxes near a boundary are SGS motions. Undue reliance on imperfect SGS modelling inhibits our ability to study turbulent flows at high Reynolds numbers. A means of

*Boundary-Layer Meteorology* **80:** 167–202, 1996.

reducing the SGS motions and at the same time increasing the resolved motions in LES is to employ multiple grids of varying resolution in the computational domain, i.e., grid nesting.

Grid nesting is often pursued for a variety of objectives. For instance, the flexibility of grid nesting, i.e., the use of multiple grids, permits analysis of flow in complex geometry. This is often the case in engineering applications (for instance Perng and Street, 1991; Henderson and Karniadakis, 1991; Danabasoglu *et al.*, 1994). On the other hand, the geometry may be simple, but the larger computational domain is subdivided because of the need to resolve small-scale physics. Grid nesting, in a variety of forms, as practiced in numerical simulation of geophysical flows and weather prediction is a means of resolving a wider range of scales than can be typically captured with a single fixed grid. This then allows one to study the interaction between flow regimes of widely disparate length scales. Nested grids have been used in geophysical applications to study supercell storms (Skamarock and Klemp, 1993), flow over topography (Clark and Hall, 1991), downslope windstorms (Clark and Farley, 1984) and nested grid technology is a central ingredient in numerical weather prediction (Phillips and Shukla, 1973), and in other mesoscale models (Walko *et al.*, 1995, Grell *et al.*, 1994).

The objective of this paper is to apply grid nesting techniques to large-eddy simulation of planetary boundary-layer turbulence, and to study the effects of high resolution in the surface-layer region. Grid nesting reduces the grid spacing and thereby increases the resolved eddy energy and fluxes and lessens the dependence on the SGS model. In the context of LES, grid nesting is expected to present new problems because of its focus on turbulent flows, turbulent flows near boundaries, and the use of nonlinear grid dependent parameterizations for SGS physics. For instance, our SGS model uses an eddy viscosity $\nu_t$ that depends on the SGS energy and the mesh spacing. It should be noted that many of the cited references use large constant eddy viscosities as SGS parameterizations. These types of SGS parameterizations, although satisfactory for their particular application, are not well suited to the simulation of turbulent flows.

The proposed grid nesting scheme uses fixed overlapping grids; the location of the nested grids is part of the problem specification. Our strategy for coupling the solutions on the different grids relies on the explicit nature of the solution procedure and determines the pressure "by an elliptic procedure" over all meshes. The proposed method evaluates the momentum equations on each mesh and incorporates the information from the nested meshes into the source term of the Poisson equation for the pressure on the coarsest mesh. A global solution of this Poisson equation is found by taking advantage of horizontal periodic boundary conditions. The net effect of this solution procedure is to couple the coarse and nested meshes. Once the pressure is determined the velocity field on the different meshes at the new time step can be constructed. A consequence of this procedure is that turbulent fluxes of momentum and heat are conserved and the velocity fields match in the common region of the different grids. Our use of pressure to achieve a matching of fine and coarse meshes however, prevents us from using temporal refinement, i.e., the same minimum time step is used for all meshes. In the current paper, we adopt the nomenclature of Clark and Hall (1991) and refer to solutions as either "one-way" interaction, i.e., when the fine grid is driven solely by coarse mesh boundary conditions with no feedback from the fine grid or "two-way" interaction, i.e., when the fine mesh solution is incorporated in the coarse mesh.

It should be noted that the proposed nesting scheme differs from the method advocated by Clark and Hall (1991). In a series of benchmark experiments, they compare results from so called "post-insertion", i.e., where fine mesh resolved fields are simply inserted into the coarse mesh, and from a "pressure defect correction" method which matches the pressure in the different meshes. Clark and Hall (1991) show that the two methods produce identical results for resolved low Reynolds number flows, and further point out that post-insertion has advantages in that it allows temporal refinement on the fine mesh and is simplier to implement. We initially pursued post-insertion but found that to be properly applied in a LES both the resolved and SGS motions should be post-inserted into the coarse mesh in order to conserve the total flux from the fine grid. This adds considerable coding complexity and is slightly more expensive than the alternate nesting method described in this paper.

## 2. Governing Equations

In LES, equations for the large scale (resolved) motions are obtained from the fundamental conservation laws by the convolution of the velocity, pressure and temperature fields with a spatial filter function. The equations governing the resolved motions are

$$\nabla \cdot \bar{\mathbf{u}} = 0, \tag{1}$$

$$\frac{\partial \bar{\mathbf{u}}}{\partial t} = \bar{\mathbf{u}} \times \bar{\boldsymbol{\omega}} - \nabla \bar{\pi} - \nabla \cdot \boldsymbol{\tau}^{\dagger} + \frac{\mathbf{g}}{\theta_0}(\bar{\theta} - \theta_0) + \mathbf{f} \times (\mathbf{U}_g - \bar{\mathbf{u}}), \tag{2}$$

$$\frac{\partial \bar{\theta}}{\partial t} = -\nabla \cdot (\bar{\theta} \bar{\mathbf{u}}) - \nabla \cdot \boldsymbol{\tau}_{\theta}^{\dagger}. \tag{3}$$

In the above, the velocity vector $\bar{\mathbf{u}}$ has components $(\bar{u}, \bar{v}, \bar{w})$ or $(\bar{u}_1, \bar{u}_2, \bar{u}_3)$ in the coordinate directions $(x, y, z)$ or $(x_1, x_2, x_3)$, the vorticity vector $\bar{\boldsymbol{\omega}} = \nabla \times \bar{\mathbf{u}}$, the reference potential temperature is $\theta_0$, the gravitational vector $\mathbf{g} = (0, 0, g)$, the Coriolis vector $\mathbf{f} = (0, 0, f)$, the geostrophic wind vector $\mathbf{U}_g = (U_g, V_g, 0)$, and $\bar{\theta}$ is the virtual potential temperature. The averaged resolved motions within a grid volume are denoted by an overbar, $\overline{(\ )}$. The generalized pressure $\bar{\pi}$ is (Moeng, 1984)

$$\bar{\pi} = \frac{\bar{p}}{\rho_0} + \frac{2}{3} e + \frac{\bar{\mathbf{u}} \cdot \bar{\mathbf{u}}}{2}, \tag{4}$$

where $\bar{p}$ is the resolved pressure, $\rho_0$ is the density and $e$ is the SGS energy. Mean pressure gradients are externally imposed by the specification of the geostrophic wind. In the above expressions $\boldsymbol{\tau}^{\dagger}$ and $\boldsymbol{\tau}_{\theta}^{\dagger}$ are SGS terms.

Equations (1)–(3) along with appropriate boundary conditions uniquely determine the resolved motions once the SGS fluxes are prescribed. The SGS model used here was first proposed by Deardorff (1980), implemented by Moeng (1984), and was further modified by Sullivan *et al.* (1994) to yield more accurate agreement with Monin–Obukhov (M–O) similarity theory in the vicinity of a bounding surface.

## 3. Computational Method

Our numerical method solves Equations (1)–(3) in a computational box with external forcing and boundary conditions representative of an atmospheric or oceanic PBL. The basic approach for atmospheric PBLs was developed by Moeng (1984) and extensions to the oceanic regime are described in McWilliams *et al.* (1993) and McWilliams *et al.* (1996). Here we generalize the numerical method in terms of how the vertical velocity boundary conditions are imposed, allow for communication between overlapping nested meshes, and improve the time integration scheme as described in following sections.

The numerical method is identical for all meshes and is a mixed spectral-finite difference scheme with solution variables advanced in physical space. Horizontal derivatives are evaluated with pseudospectral methods while vertical derivatives are approximated with second order centered finite differences. A staggered grid is used in the vertical direction with the location of $U$ grid points midway between neighboring $W$ grid points. Variables stored at $U$ grid points are the velocity components $\bar{u}$ and $\bar{v}$, virtual potential temperature $\bar{\theta}$, and pressure $\bar{p}$. Vertical velocity $\bar{w}$ and SGS energy $e$ are stored at $W$ locations.

The grid architecture consists of a single outer (or coarse) grid, and nested (or fine) grids, which overlap the coarse grid in some common region. The nested domains can be arbitrarily positioned in the vertical direction, but are required to span the same horizontal extent, i.e, the same $x - y$ dimensions, as the outer grid. This constraint is imposed because of the desire to use horizontal periodic boundary conditions for all meshes; different spectral basis functions would be required if this condition was not imposed. We also allow the possibility of multiple nested meshes, i.e., any nested mesh can itself contain even finer meshes. The use of a staggered vertical mesh impacts the nesting procedure since the bounds of the fine mesh need to coincide with some portion of the outer coarse grid; here it is natural to collocate the upper and lower faces of the fine mesh at coarse mesh $W$ locations. This choice of grid geometry permits the same solution procedure to be followed independent of the mesh with only a slight change to the form of the upper and lower boundary conditions.

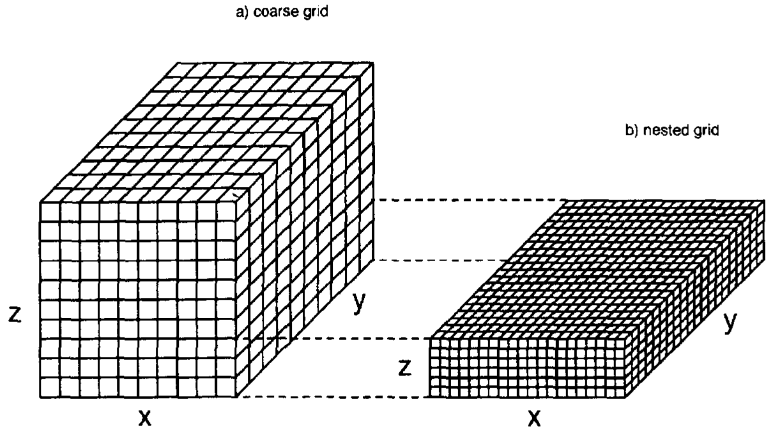

*Figure 1.* Sketch illustrating grid architecture in (a) coarse and (b) fine grids for coarse-to-fine spacing of 2 : 1 in all directions. In the $x - y$ plane all mesh variables are evaluated at the intersection of grid lines, while in the $x - z$ plane $U$ and $W$ variables are staggered.

A sketch showing the orientation of outer and nested grids in a 3-D perspective for a coarse-to-fine grid spacing $\Delta x_c/\Delta x_f = \Delta y_c/\Delta y_f = \Delta z_c/\Delta z_f = 2$ (the subscripts $c$ and $f$ denote coarse and fine meshes) is given in Figure 1. The location of the staggered $U$ and $W$ nodes for an arbitrary vertical column passing through the coarse and fine meshes is shown in Figure 2. Here the ratios $\Delta x_c/\Delta x_f$ and $\Delta y_c/\Delta y_f$ can take on arbitrary values greater than unity, while in the $z$ direction the ratio $\Delta z_c/\Delta z_f$ is required to be an integer.

The imposed boundary conditions are unique to the particular mesh. In the coarse grid, boundary conditions at the surface are no slip conditions with M–O similarity theory used to relate conditions at the first computational grid point to the surface conditions. At the upper boundary of the coarse grid, the boundary conditions are zero SGS turbulence fields, $\partial\bar{u}/\partial x = 0$, $\partial\bar{v}/\partial y = 0$, and $\partial\bar{\theta}/\partial z$ = constant and a radiation boundary condition (Klemp and Durran, 1983) which ties together vertical velocity and pressure. In the fine mesh, Dirichlet conditions derived from the coarser mesh are used for $\bar{\mathbf{u}}$, $e$, and $\bar{\theta}$ variables along the upper and lower faces. However, if the lower boundary of the nested grid happens to coincide with a solid surface then M–O boundary conditions are used similar to the coarse grid. For all meshes, the flow is assumed to be statistically and horizontally homogeneous and thus periodic boundary conditions are used along the sidewalls of the computational domain.

A grid nesting algorithm requires inter-grid communication in order to advance the solution on the different meshes. The inherent different grid densities dictate that algorithms be available for interpolation of coarse mesh data to the fine grid and similarly averaging of the fine mesh data to the coarse grid. For the latter operation we have coined the term *anterpolation*. We define anterpolation as restriction using an operator that is an inverse for any previous interpolation for sufficiently smooth

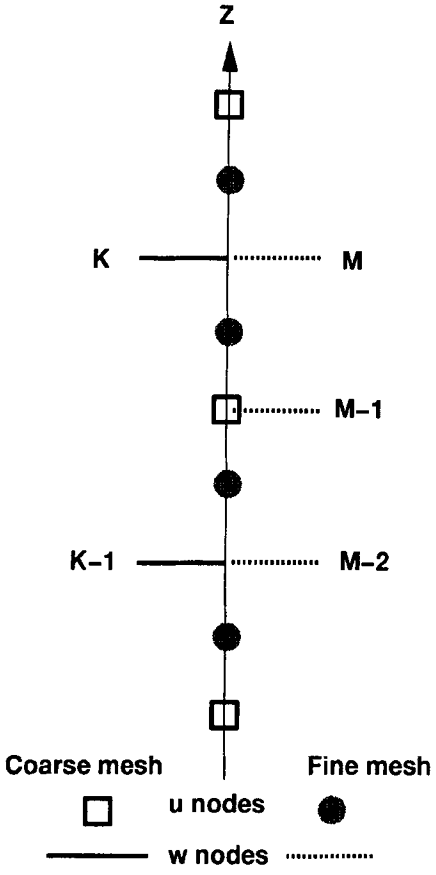

*Figure 2.* Position of grid nodes in coarse and fine grid for an arbitrary vertical column passing through both grids, coarse to fine spacing of 2 : 1, upper boundary of fine grid node $M$ coincides with coarse grid node $K$.

fields. In the text, an interpolation operation is indicated by $\check{(\,)}$ and anterpolations by $\widetilde{(\,)}$. These operations are carried out using a combination of spectral filtering in the $x - y$ directions and when required simple averaging in the $z$ direction. The particulars of the interpolation and anterpolation schemes are described in Appendix A.

### 3.1. TIME STEPPING SCHEME

The main elements of the time integration scheme are briefly mentioned to better understand the pressure solution scheme described in Section 3.2, the nested grid solution matching outlined in Section 3.3, and the determination of the time step for cases with multiple meshes of different density. We have adopted the explicit third-order accurate multi-stage Runge–Kutta scheme (RK3) with a variable time step developed by Spalart *et al.* (1991), with some modifications. Previously, Moeng (1984) employed a second order accurate Adams–Bashforth (AB2) method with a fixed time step as the time integration scheme. In our implementation of RK3, all terms in the momentum equations are treated explicitly owing to the complexity of the viscous term and because of the computational similarities between explicit RK3 and AB2, i.e., only modest changes to the code are required to implement RK3.

In the RK3 method, the rule for advancing any of the velocity components, $\bar{u}_i|^n$, at time $t$ to $\bar{u}_i|^{n+1}$ at time $t + \Delta t$, consists of three substeps (or stages):

$$\bar{u}_i|' = \bar{u}_i|^n + \Delta t[\gamma_1 R_i|^n + \zeta_1 R_i|^{n-1}], \tag{5}$$

$$\bar{u}_i|'' = \bar{u}_i|' + \Delta t[\gamma_2 R_i|' + \zeta_2 R_i|^n], \tag{6}$$

$$\bar{u}_i|^{n+1} = \bar{u}_i|'' + \Delta t[\gamma_3 R_i|'' + \zeta_3 R_i|'], \tag{7}$$

where

$$R_i = r_i - \frac{\delta \bar{\pi}}{\delta x_i}. \tag{8}$$

Here $\delta/\delta x_i$ is the discrete divergence operator and the right-hand side term $r_i$ includes all terms of the momentum equations (2) except the pressure $\bar{\pi}$. Spalart *et al.* (1991) chose the weights so that the entire scheme is third-order accurate and suggest:

$$\gamma_1 = \frac{8}{15},\ \gamma_2 = \frac{5}{12},\ \gamma_3 = \frac{3}{4},\ \zeta_1 = 0,\ \zeta_2 = -\frac{17}{60},\ \zeta_3 = -\frac{5}{12}. \tag{9}$$

A Courant–Friedrichs–Lewy (CFL) number of 0.21 was typically used at each stage (or CFL=0.63 for an entire step); this CFL number is more than a factor of 2 larger than for AB2. Since the CFL number is held constant, the maximum allowable time step is computed dynamically at each iteration. Here the CFL number is defined as

$$\mathrm{CFL} = \max\left[\frac{|\bar{u}|}{\Delta x}, \frac{|\bar{v}|}{\Delta y}, \frac{|\bar{w}|}{\Delta z}\right]\Delta t, \tag{10}$$

where the grid spacings are $\Delta x$, $\Delta y$ and $\Delta z$. The same CFL test is used for all grids and for both atmospheric and oceanic simulations. In the case of nested grids, the minimum time steps on the fine and coarse meshes $\Delta t_f$ and $\Delta t_c$ are first found from (10) and their minimum value $\Delta t = \min(\Delta t_f, \Delta t_c)$ is used for all meshes. Thus the same time step is used for all grids. The adaptive time stepping algorithm used here for the nested grid simulations has clear advantages over a fixed time step. In the case of atmospheric simulations where $u \to 0$ as $z \to 0$, and $u \to U_g$ as $z \to Z_l$, a

Galilean transformation is applied to the coordinate system such that the grids are advected in the $x$ direction at a constant speed equal to 1/2 of the geostrophic wind to further increase the permissible time step. The conservation equation for virtual potential temperature Equation (3) and the prognostic equation for the SGS kinetic energy (Moeng, 1984; Sullivan *et al.*, 1994) are time advanced with the same scheme as the velocity variables, but without the complications associated with the pressure. At each stage of the RK3 integration, the same boundary conditions described in Sections 3 and 3.2 are used.

### 3.2. THE PRESSURE EQUATION AND ITS BOUNDARY CONDITIONS

The pressure field is determined to maintain $\nabla \cdot \bar{\mathbf{u}} = 0$ at each stage of the RK3 integration. Here we describe details of the pressure computation at the initial stage of the RK3 method; identical steps are followed at other RK3 substeps. Given

$$\left.\frac{\partial \bar{u}_i}{\partial x_i}\right|' = 0, \tag{11}$$

the pressure field is the solution of

$$\left.\frac{\delta^2 \bar{\pi}}{\delta x_i^2}\right|^n = \left.\frac{1}{\Delta t \gamma_1}\frac{\delta \bar{u}_i}{\partial x_i}\right|^n + \left.\frac{\delta r_i}{\delta x_i}\right|^n + \left.\frac{\zeta_1}{\gamma_1}\frac{\delta R_i}{\delta x_i}\right|^{n-1}, \tag{12}$$

which follows from applying $\delta/\delta x_i$ to the discrete form of the momentum Equations (5). Vertical boundary conditions for the pressure equation for the coarse and all nested meshes follow from the application of Equation (11) at the boundary nodes. For the staggered vertical grid used, with nodes $m = 0, 1, \ldots, M$ as shown in Figure 2, the vertical discretization of (11) at the upper boundary is

$$\left[\frac{\delta \bar{u}_1}{\delta x_1} + \frac{\delta \bar{u}_2}{\delta x_2}\right]'_{M-1/2} + \frac{1}{\Delta z}\left[\bar{u}_3\,|'_M - \bar{u}_3|'_{M-1}\right] = 0. \tag{13}$$

Substitution of the time discretizations for $\bar{u}_1|'_{M-1/2}$, $\bar{u}_2|'_{M-1/2}$, and $\bar{u}_3|'_{M-1}$ from Equation (5) into Equation (13) leads to the pressure boundary condition equation at the upper node $M - 1/2$,

$$\begin{aligned}
&\left[\frac{\delta^2 \bar{\pi}}{\delta x_1^2} + \frac{\delta^2 \bar{\pi}}{\delta x_2^2}\right]^n_{M-1/2} - \left.\frac{1}{\Delta z}\frac{\delta \bar{\pi}}{\delta x_3}\right|^n_{M-1} \\
&= \frac{1}{\Delta t \gamma_1 \Delta z}(\bar{u}_3|'_M - \bar{u}_3|^n_{M-1}) + \frac{1}{\Delta t \gamma_1}\left[\frac{\delta \bar{u}_1}{\delta x_1} + \frac{\delta \bar{u}_2}{\delta x_2}\right]^n_{M-1/2} \\
&+ \left[\frac{\delta r_1}{\delta x_1} + \frac{\delta r_2}{\delta x_2}\right]^n_{M-1/2} - \left.\frac{r_3}{\Delta z}\right|^n_{M-1} + \frac{\zeta_1}{\gamma_1}\left[\frac{\delta R_1}{\delta x_1} + \frac{\delta R_2}{\delta x_2}\right]^{n-1}_{M-1/2}
\end{aligned}$$

$$-\frac{\zeta_1}{\gamma_1}\frac{R_3}{\Delta z}\bigg|_{M-1}^{n-1}. \tag{14}$$

A similar expression can also be written for the lower boundary by applying the divergence free condition at the nodes $m = 0$, 1/2 and 1:

$$\left[\frac{\delta^2\bar{\pi}}{\delta x_1^2}+\frac{\delta^2\bar{\pi}}{\delta x_2^2}\right]_{1/2}^{n}+\frac{1}{\Delta z}\frac{\delta\bar{\pi}}{\delta x_3}\bigg|_{1}^{n}$$

$$=\frac{1}{\Delta t\gamma_1\Delta z}(\bar{u}_3|_1^n-\bar{u}_3|_0^{\prime})+\frac{1}{\Delta t\gamma_1}\left[\frac{\delta\bar{u}_1}{\delta x_1}+\frac{\delta\bar{u}_2}{\delta x_2}\right]_{1/2}^{n}$$

$$+\left[\frac{\delta r_1}{\delta x_1}+\frac{\delta r_2}{\delta x_2}\right]_{1/2}^{n}+\frac{r_3}{\Delta z}\bigg|_{1}^{n}+\frac{\zeta_1}{\gamma_1}\left[\frac{\delta R_1}{\delta x_1}+\frac{\delta R_2}{\delta x_2}\right]_{1/2}^{n-1}+\frac{\zeta_1}{\gamma_1}\frac{R_3}{\Delta z}\bigg|_{1}^{n-1}. \tag{15}$$

Some general observations about Equations (14) and (15) are worth mentioning. First, the pressure boundary conditions derived above are applicable to meshes which have natural physical boundaries such as a solid surface and also to meshes with an interior boundary, i.e., where the vertical boundary of a particular mesh lies within the interior of another mesh. Also, when the pressure gradients $\delta\bar{\pi}/\delta x_3|_{M-1}^{n}$ and $\delta\bar{\pi}/\delta x_3|_1^n$ are expanded, only nodes within the interior of the computational domain are referenced. The pressure boundary conditions (14) and (15) can then be implemented if the vertical velocity along the upper and lower boundaries can be specified at the new time level, i.e, provided $\bar{u}_3|_0^{\prime}$ and $\bar{u}_3|_M^{\prime}$ are known. In our solution method, these particular vertical velocities are in fact known for the coarse and nested meshes, and thus the pressure is uniquely determined. For instance in the coarse grid, at $z = 0$ the noflow condition $\bar{w}(x, y, 0, t) = 0$ is used. Meanwhile, for nested grids, where the vertical boundaries are not physical boundaries, these same vertical velocities are also known at the upper and lower boundaries of the fine mesh since coarse grid variables are determined at the new time level prior to updating the fine mesh variables (see Section 3.3). In the coarse grid, the radiation boundary condition at the upper boundary couples vertical velocity and pressure and is used in place of Equation (14). Thus, a general method for specifying the pressure boundary conditions on any mesh is available.

The Poisson equation for the pressure is solved using standard methods. First, Equation (12) and the boundary conditions (14) and (15) are Fourier transformed in the $x$ and $y$ directions which leads to a one-dimensional Helmholtz problem in the vertical direction for each pair of horizontal wavenumbers. Expansion of the centered vertical differencing operator $\delta^2\bar{\pi}/\delta x_3^2$ results in a tridiagonal system of algebraic equations which is inverted using a vectorized version of the Thomas algorithm. After the above step is repeated for all wavenumbers the resulting wave-space pressure solutions are then inverse Fourier transformed to get the physical space pressure. $\nabla \cdot \bar{\mathbf{u}} = 0$ is satisfied to machine precision on all grids at each stage of the time stepping scheme.

### 3.3. MATCHING OF COARSE AND FINE GRID SOLUTIONS

Velocity, potential temperature and SGS energy boundary conditions are also required on the upper and lower bounds of the nested meshes. These boundary conditions are Dirichlet conditions derived from coarse grid variables. Along the upper boundary of the nested grid, the fine mesh $\bar{w}$ and $e$ at node $M$ are determined by $x - y$ spectral interpolation of coarse mesh vertical velocity and SGS energy at node $K$ (see Figure 2); thus $\bar{w}|^n_M = \breve{W}|^n_K$ and $e|^n_M = \breve{E}|^n_K$, here uppercase letters denote coarse mesh variables. Fine mesh variables at node $M = 1/2$ are found by spectrally interpolating coarse mesh variables at nodes $K + 1/2$ and $K - 1/2$ and then averaging, for example $\bar{u}|^n_{M+1/2} = -\bar{u}|^n_{M-1/2} + \breve{U}|^n_{K+1/2} + \breve{U}|^n_{K-1/2}$. Similar Dirichlet conditions are used on the lower boundary of the nested mesh except for the case where the lower boundary is a solid surface.

In order to provide for two-way interaction between the meshes, information from the nested mesh needs to be incorporated in the outer mesh. Our algorithm for two-way interaction is referred to as pressure matching (PM), and follows from a compatibility condition between the coarse and fine mesh fields at the next time step in the integration. At each stage of the integration we equate the coarse mesh field and its fine mesh counterpart anterpolated to the coarse grid, i.e., in the overlap region we set $U_i|' = \tilde{\bar{u}}_i|'$. In terms of the general rule for advancing the velocity field, for example Equation (5), this matching condition between coarse and fine meshes is

$$U_i|' \equiv \tilde{\bar{u}}_i|' = \tilde{\bar{u}}_i|^n + \Delta t \left[ \gamma_1 \tilde{r}_i|^n - \gamma_1 \left. \frac{\delta \tilde{\bar{\pi}}}{\delta x_i} \right|^n + \zeta_1 \tilde{R}_i|^{n-1} \right] . \tag{16}$$

Equation (16) is satisfied provided a consistent pressure $\tilde{\bar{\pi}}|^n$ is found. The correct pressure can be determined by using anterpolated fine mesh velocity and right-hand sides in the Poisson equation for the global coarse mesh pressure. In other words, in the overlap region we insert $\tilde{\bar{u}}|^n$, $\tilde{r}_i|^n$, and $\tilde{R}_i|^{n-1}$ into the source term of Equation (12) for the coarse mesh pressure. In this manner, the effects of the fine mesh solution are fully accounted for in the coarse mesh solution prior to the next RK3 substep. Notice that because anterpolated fine mesh variables are used in the source term of Equation (12), the same general solution procedure for the pressure can be used for cases with and without interaction. Once the coarse mesh pressure is found the coarse mesh velocity field $U_i|'$ at the next substep is constructed from Equation (5).

The last step in the PM method is computation of the pressure and velocity field at the next substep in the fine mesh. Because the coarse mesh vertical velocity field $W|'_K$ is now known, the fine mesh pressure is simply computed using the scheme described in Section 3.2. Once the fine mesh pressure is found, the fine mesh velocity field at the new time step $\bar{u}_i|'$ can be computed, again according to Equation (5). The above grid nesting procedure ensures that the anterpolated fine mesh velocity field matches its coarse mesh counterpart in the overlap region. In addition, the current nesting method automatically conserves the total flux from the fine grid, i.e., the sum of resolved and SGS fluxes from the fine grid is felt in the coarse mesh, as shown in Section 3.5. The virtual potential temperature on the nested grid is accounted for in the outer grid by inserting the anterpolated fine mesh potential temperature and its right-hand side into the coarse grid at each stage of the integration.

A detail remains with regard to the nesting scheme described above. In order to prevent discontinuous behaviour in the SGS eddy viscosity at the grid interface we adopted a blending rule for the length scale which appears in the eddy viscosity model. Recall that the eddy viscosity function used involves both the SGS energy $e$ and a length scale $\Delta$ (Moeng, 1984; Sullivan *et al.*, 1994). At the grid interface, our boundary conditions for SGS emergy already equate the coarse and fine mesh SGS energy, and thus to maintain a smoothly varying eddy viscosity the length scale $\Delta$ was continuously varied from its value in the coarse grid $\Delta_c$ to its final value in the fine grid $\Delta_f$ over a few gridpoints. The blending rule for $\Delta(z)$ is a cubic polynomial that matches $\Delta_c$ and $\Delta_f$ at the endpoints of the blending interval with zero slope. $\Delta(z) = \Delta_c$ at the grid interface and all blending is done in the fine grid. By requiring that $\Delta(z) = \Delta_c$ at the grid interfaces the eddy viscosity in the fine grid is then equal to its coarse grid value. Furthermore, this blending procedure imposes continuity on the SGS dissipation $\epsilon$ since $\epsilon = e^{3/2}/\Delta$ (Moeng, 1984), and permits quite large jumps in grid density between coarse and fine grids.

### 3.4. RELATIONS BETWEEN EDDY FLUXES ON FINE AND COARSE GRIDS

An LES that employs grid nesting must treat both resolved and SGS fluxes in the region where the grids overlap. Here we develop the relationship that can be used to convert total eddy fluxes on the fine mesh into total eddy fluxes on the overlapping coarse mesh.

The proper expression for conservation of total flux between grids of different density follows by applying different spatial filters to the governing equations. For any mesh, the average effective grid spacing $\Delta$ is a natural choice for the filter cutoff scale, i.e., only motions with scales larger than $\Delta$ can be adequately resolved. In terms of the actual mesh spacings, $\Delta = ((9/4)\Delta x \Delta y \Delta z)^{1/3}$ which accounts for de-aliasing of the upper 1/3 of the wavenumbers. For a computation with multiple meshes, we assign filters to the nested grid $\bar{()}$, associated with the fine mesh length scale $\Delta_f$, and to the outer grid $\widetilde{()}$ associated with the coarse mesh length scale

$\Delta_c$. Here $\Delta_c \geq \Delta_f$. The SGS momentum and heat fluxes (or stresses) for the fine mesh are respectively;

$$\boldsymbol{\tau}^{\dagger} \equiv \tau_{ij} = \overline{u_i u_j} - \bar{u}_i \bar{u}_j, \tag{17}$$

and

$$\boldsymbol{\tau}_{\theta}^{\dagger} \equiv \tau_{\theta j} = \overline{\theta u_j} - \bar{\theta} \bar{u}_j, \tag{18}$$

while their counterparts for the coarse grid are

$$\mathbf{T}^{\dagger} \equiv T_{ij} = \widetilde{\overline{u_i u_j}} - \tilde{\bar{u}}_i \tilde{\bar{u}}_j, \tag{19}$$

and

$$\mathbf{T}_{\theta}^{\dagger} \equiv T_{\theta j} = \widetilde{\overline{\theta u_j}} - \tilde{\bar{u}}_j \tilde{\bar{u}}_j. \tag{20}$$

Filtering (or anterpolating) Equation (17) to the coarse mesh resolution, and combining the result with Equation (19) leads to an expression for the coarse mesh SGS fluxes in terms of fine mesh variables

$$T_{ij} = \tilde{\tau}_{ij} + (\widetilde{\bar{u}_i \bar{u}_j} - \tilde{\bar{u}}_i \tilde{\bar{u}}_j). \tag{21}$$

Contraction of this tensor produces an expression for the coarse mesh SGS energy

$$E = \tilde{e} + \frac{1}{2}(\widetilde{\bar{u}_i \bar{u}_i} - \tilde{\bar{u}}_i \tilde{\bar{u}}_i). \tag{22}$$

Similar manipulations leads to an expression for the coarse mesh heat flux

$$T_{\theta i} = \tilde{\tau}_{\theta i} + (\widetilde{\bar{\theta} \bar{u}_i} - \tilde{\bar{\theta}} \tilde{\bar{u}}_i). \tag{23}$$

How Equations (21)–(23) are satisfied by our nesting scheme is described in the next section.

### 3.5. COARSE GRID SGS PHYSICS

Expressions (21), (22), and (23) describe how SGS fluxes and energy in the coarse grid are related to motions in the fine grid. In these equations, the coarse mesh SGS flux or energy has contributions from fine mesh SGS motions and resolved eddies. The first term on the right-hand side of Equations (21), (22), and (23) is the contribution to the coarse mesh SGS flux or energy from its fine mesh counterpart. Since this term is typically modelled in terms of fine mesh resolved motions it must be filtered before use on the coarse grid. The second term on the right-hand side of Equations (21), (22) and (23) only involves fine mesh resolved motions, and represents conversion of fine mesh resolved motions of length scale $l$ which fall between $\Delta_f \leq l \leq \Delta_c$ into coarse mesh SGS fluxes. In other words, motions of length scale $l$ which fall between $\Delta_f \leq l \leq \Delta_c$ in the nested grid are no longer resolved in the outer grid, but appear naturally as SGS motions in the coarse mesh. Since the coarse mesh resolved velocity and potential temperature are $U_i = \tilde{\bar{u}}_i$ and $\Theta = \tilde{\bar{\theta}}$, Equations (21), (22), and (23) can also be interpreted as conservation rules for total momentum flux, total kinetic energy and total heat flux between a nested and coarser mesh. This balance applies on a gridpoint basis and also to the ensemble average.

Equations (21), (22) and (23) are the conservation laws that should be obeyed by a grid nesting scheme. The SGS motions on a coarse grid are not simply obtained by substituting the anterpolated fine mesh resolved fields $\tilde{\bar{u}}_i$ and $\tilde{\bar{\theta}}$ into the SGS model. The nonlinearity of most SGS models and the nonlinear transfer associated with a turbulent cascade process require that Equations (21), (22), and (23) be used in order to maintain conservation of fluxes and energy on the coarse grid. Inspection of our PM method (see Section 3.3) reveals that the above total turbulent flux conservation rules are *implicitly enforced* when the fine mesh right-hand sides $r_i$ are anterpolated to the coarse grid; note that $r_i$ is proportional to the divergence of the total flux, i.e., $r_i \sim \nabla \cdot [\tau_{ij} + \bar{u}_i\bar{u}_j]$ so that $\tilde{r}_i \sim \nabla \cdot [\tilde{\tau}_{ij} + \widetilde{\bar{u}_i\bar{u}_j}] = \nabla \cdot [T_{ij} + U_iU_j]$. An advantage of the PM method of Section 3.3 is that only a single evaluation of the SGS model on the fine grid is required in order to enforce the total flux conservation rules. Grid nesting methods which rely on post-insertion of fine mesh data into the coarse grid should anterpolate both the fine mesh resolved and SGS motions to the coarse grid in order to conserve the total flux from the fine grid. In other words, Equations (21)–(23) need to be explicitly enforced by a post-insertion method which is computationally complex.

It should be noted that approximations to the conservation rules (21), (22), and (23) have been employed in other nesting methods associated with mesoscale models. For instance, Skamarock and Klemp (1993), Clark and Hall (1991) and Walko *et al.* (1995) all assume that in their nested applications the SGS motions in the coarser grid are simply evaluated from the resolved motions in the coarse grid; in other words, $T_{ij}$ in (21) is approximated by the SGS model in the coarse mesh which is a reasonable assumption when the resolved motions are much greater than the SGS motions. Near boundaries however the resolved flux disappears, the SGS contributions are large, and consequently this approximation breaks down.

Finally, we are fully aware that Equation (21) is formally identical to Germano's identity (Germano *et al.*, 1991) which is used to develop dynamic SGS models. Thus, this important relation also naturally appears in a nested grid LES application and is implicitly enforced by our nesting method.

### 3.6. SOLUTION ALGORITHM

The details associated with our nested solution procedure are described in Sections 3.1 through 3.5. An overview of the basic steps are included here to summarise the method.

1. Coarse mesh solution variables are advanced up to a certain time level $n$ where it is desired to turn on the nesting solution. Typically, this time is selected such that the coarse solution is reasonably spun up to a fully developed turbulent state.
2. Coarse mesh variables at time level $n$ are spatially interpolated onto the nested mesh along the upper and lower faces of the nested mesh, and serve as fine mesh boundary conditions.
3. Right-hand sides of the governing equations for the velocity field (minus the pressure), potential temperature, and SGS energy are computed for all fine and coarse grids, e.g., see Equation (5) for the velocity. At this step either one-way or two-way interaction can take place.
4. For two-way interaction, the right-hand sides of the fine mesh equations for $u$, $v$, $w$, and $\theta$ from step 3 are anterpolated to the coarse grid. Thus, in the overlap region coarse grid information is replaced by anterpolated fine grid information. The coarse mesh solution then proceeds in the usual manner.
5. Solve the Poisson equation (12) for the coarse grid pressure (with the anterpolated fine mesh fields in the overlap region if two-way intertaction) and construct the coarse mesh velocity and temperature fields at the new time step.
6. Use the coarse mesh vertical velocity at the new time step $W|_K^{\prime}$ to determine the fine mesh pressure boundary conditions (14) and (15), solve for the fine mesh pressure using (12), and update the fine mesh velocity and temperature fields.
7. In the overlap region, construct the coarse mesh SGS energy $E$ from the fine mesh fields using Equation (22) for later analysis.
8. For one-way interaction skip steps 4 and 7.
9. Repeat steps 2–8 for all RK3 substeps.

## 4. Examples and Results

### 4.1. SIMULATIONS

In order to test the nesting algorithm developed in Section 3, a series of simulations with a fixed outer grid and a single nested grid in the surface layer of varying resolution were performed for an atmospheric PBL. The intent of these simulations is twofold; (1) to illustrate that the method works and produces smooth solutions across the nested interface, and (2) to study the consequences of surface-layer nesting on both surface layer and mixed-layer PBL physics. Another example of the present grid nesting method applied to an oceanic PBL is briefly described in McWilliams *et al.* (1996).

Our study of the effects of one-way and two-way grid nesting in the surface layer utilizes both qualitative and quantitative measures. A qualitative impression of the scale and intensity of the turbulent motions is obtained from instantaneous flow pictures while the effects of grid nesting are quantified by comparing ensemble statistics (variances, fluxes and spectra) inside and outside the surface layer of the PBL. Ensemble statistics are the correct quantitative measures for judging the effects of nesting but are clouded by the uncertainties associated with the averaging process. Because of the stochastic nature of turbulence we have no exact standard for comparison, but expect that our solutions with high resolution (smaller SGS motions) are more faithful representations of high Reynolds number turbulent flows than simulations with larger SGS motions. In order to further clarify this issue we plan to compare statistics from our fine mesh nested solutions to a benchmark LES of fine resolution everywhere in the domain in the future.

The particulars of the simulations are presented in Tables I and II. Parameters in these tables are; the geostrophic wind ($U_g$, $V_g$), surface heat flux $Q_0$, Coriolis parameter $f$, initial capping inversion height $z_i$, computational domain size ($X_l$, $Y_l$, $Z_l$), surface friction velocity $u_*$, convective velocity scale $w_*$, temperature scale $\theta_* = Q_0/w_*$, Obukhov length $L$, large eddy turnover time $\tau_e = z_i/w_*$, and the location of of the upper boundary of the nested grid $z_u$. All the simulations were carried out for the same external forcing conditions, viz., $(U_g, V_g) = (15, 0)$ m s$^{-1}$ and $Q_0 = 0.03$ K m s$^{-1}$ ($\approx$30 W m$^{-2}$). Overall the general properties are equivalent to the simulations with strong shear and weak buoyancy described in Moeng and Sullivan (1994). The nested grid is located in the surface layer region of the PBL, and ranges from $0 \le z \le 0.18 z_i$, or in terms of gridpoints, the lowest 10 points in the outer coarse grid. Note that for case $N5$, the simulation with the finest resolution, the number of gridpoints in the $x$ and $y$ directions are each increased by a factor of 5 and in the $z$ direction by a factor of 2 compared to the outer coarse grid simulation $N1$.

The simulations were constructed by first running the coarse mesh simulation $N1$ for about 3000 steps, which corresponds to about 5300 s or about 8.3 large eddy turnover times $\tau_e$, to reach a full developed turbulent state. At this point, the flow fields from $N1$ were used to start all the simulations in Table II; each simulation was then integrated for another $7.50\tau_e$. Ensemble statistics were gathered from the last 3.5 to 4.0 turnover times of the simulations.

### 4.2. SOLUTION MATCHING IN THE SURFACE LAYER

The two-way nesting algorithm is designed such that in the overlap region, at any instant in time, coarse mesh variables are direct descendants of their fine mesh counterparts. If the two-way algorithm has been implemented correctly then the *anterpolated* fine mesh solution should match the coarse mesh solution at the same

Table I
Simulated flow properties

| | |
|---|---|
| Geostrophic wind $(U_g, V_g)$ | $(15, 0)$ m s$^{-1}$ |
| Surface heat flux $Q_0$ | 0.03 K m s$^{-1}$ |
| Coriolis parameter $f$ | $10^{-4}$ s$^{-1}$ |
| Initial capping inversion height $z_i$ | 500 m |
| Domain size $(X_l, Y_l, Z_l)$ | $(1500, 1500, 900)$ m |
| Surface friction velocity $u_*$ | 0.553 m s$^{-1}$ |
| Convective velocity scale $w_*$ | 0.788 m s$^{-1}$ |
| Temperature scale $\theta_*$ | 0.038 K |
| Obukhov length $L$ | −431.0 m |
| Large eddy turnover time $\tau_e$ | 634 s |
| Upper boundary of nested grid $z_u$ | $0.18z_i$ or 90 m |

Table II
Grid resolutions of simulations

| Case | Coarse mesh gridpoints | Coarse mesh spacing $(\Delta x, \Delta y, \Delta z)$ m | Fine mesh gridpoints | Fine mesh spacing $(\Delta x, \Delta y,, \Delta z)$ m | Interaction |
|---|---|---|---|---|---|
| $N1$ | $50 \times 50 \times 100$ | $30 \times 30 \times 9$ | | | None |
| $N2$ | $50 \times 50 \times 100$ | $30 \times 30 \times 9$ | $150 \times 150 \times 10$ | $10 \times 10 \times 9$ | One-way |
| $N3$ | $50 \times 50 \times 100$ | $30 \times 30 \times 9$ | $150 \times 150 \times 10$ | $10 \times 10 \times 9$ | Two-way |
| $N4$ | $50 \times 50 \times 100$ | $30 \times 30 \times 9$ | $150 \times 150 \times 20$ | $10 \times 10 \times 4.5$ | Two-way |
| $N5$ | $50 \times 50 \times 100$ | $30 \times 30 \times 9$ | $250 \times 250 \times 20$ | $6 \times 6 \times 4.5$ | Two-way |

instant in time. In order to test the correctness of our algorithm, 3-D fine and coarse mesh flow fields were saved and analyzed after several large eddy turnover times. Snapshots of the resolved vertical velocity field $\bar{w}$ in $x - y$ and $x - z$ planes from the coarse and nested grids for case $N3$ are pictured in Figures 3 and 4. In Figure 3, the vertical location is $z = 0.072z_i$ (or gridpoint 4 in the coarse grid) while in Figure 4 the spanwise location $y$ is at the center of the computational domain. For clarity, only a fraction of the entire vertical extent of the PBL is displayed in Figure 4a. Inspection of the results shows that nesting increases the resolved motions to an appreciable extent, the amount of small-scale resolved motion is visibly increased in Figures 3b and 4b compared to their counterparts in Figures 3a and 4a. Moreover, the anterpolated fine mesh fields shown in Figures 3c and 4c match their coarse mesh counterparts shown in Figures 3a and 4a, thus validating the general correctness of our two-way interaction algorithm. We found that all resolved velocity components, generalised pressure and potential temperature equally satisfy this same test in the overlap region.

In contrast to simulations with two-way interaction, the dynamical fields obtained from simulations with one-way interaction are not constrained to match in their common overlap region. The extent to which the coarse and nested flow fields

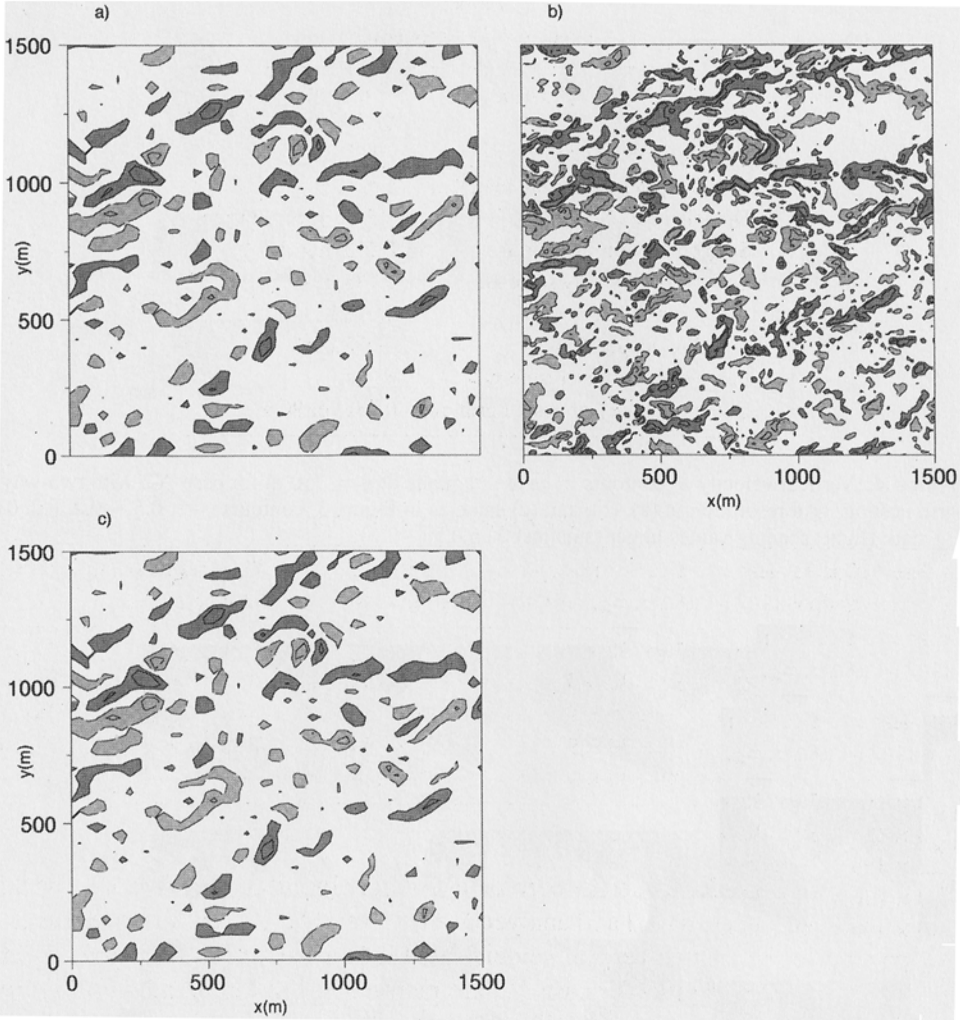

*Figure 3.* Vertical velocity $\bar{w}$ contours in an $x - y$ plane at $z = 0.072z_i$ for case $N3$ with two-way grid nesting; (a) coarse grid $50 \times 50 \times 100$, (b) nested grid $150 \times 150 \times 10$, and (c) nested grid filtered to coarse grid resolution; contours $(-1, -0.5, 0.5, 1)$, dark (light) shading values larger (smaller) than 0.5 (−0.5).

differ is illustrated in Figure 5 for an $x - z$ slice through the domain. Here the resolved vertical velocity on the different meshes is shown along with the anterpolated fine mesh field at the same time step. Inspection of the results indicates that the coarse and fine mesh $\bar{w}$ flow fields are of comparable magnitude, but otherwise differ markedly in the orientation and location of regions of strong vertical velocity. Similar results were found for other slices through the computational domain. This one-way interaction result shows that the fine mesh field, despite being driven

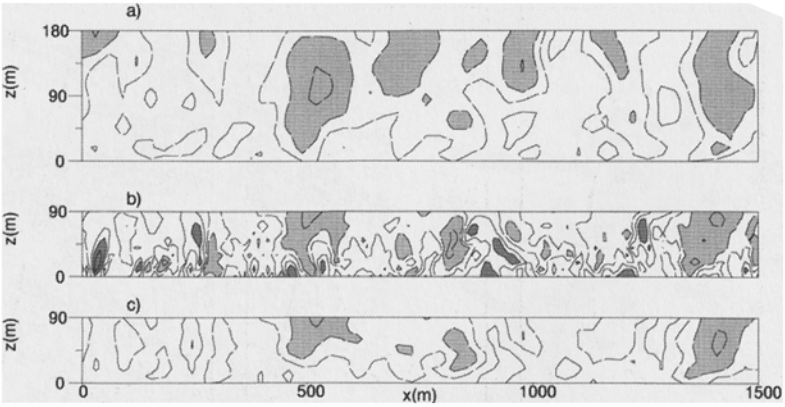

*Figure 4.* Vertical velocity $\bar{w}$ contours in an $x - z$ plane at $y = 750$ m for case $N2$ with two-way grid nesting, grid resolution in (a), (b), and (c) same as in Figure 3; contours $(-1, 0.5, -0.2, 0.2, 0.5, 1)$, dark (light) shading values larger (smaller) than 0.5 $(-0.5)$.

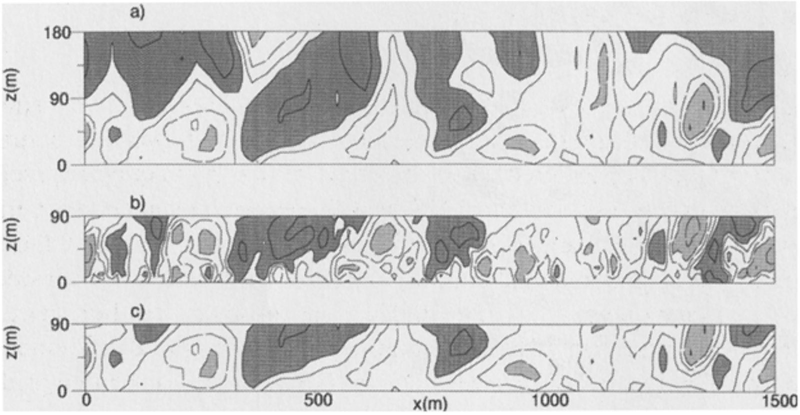

*Figure 5.* Vertical velocity $\bar{w}$ contours in an $x - z$ plane at $y = 750$ m for case $N2$ with one-way grid nesting, grid resolution in (a), (b), and (c) same as in Figure 3; contours $(-1, -0.5, -0.2, 0.2, 0.5, 1)$, dark (light) shading values larger (smaller) than 0.5 $(-0.5)$.

by coarse mesh boundary conditions, differs considerably from its coarse mesh counterpart on an instantaneous point-by-point basis away from the boundaries.

### 4.3. ENSEMBLE STATISTICS IN THE SURFACE LAYER

Ensemble averaged heat flux profiles in the surface-layer region for cases $N2$, $N3$, and $N5$ are depicted in Figure 6. In this figure, the vertical coordinate is normalized by $z_i$, while the total $\langle \bar{\theta} \bar{w} \rangle_{\text{total}}$ resolved $\langle \bar{\theta} \bar{w} \rangle_{\text{R}}$, and SGS $\langle \bar{\theta} \bar{w} \rangle_{\text{SGS}}$ heat fluxes are

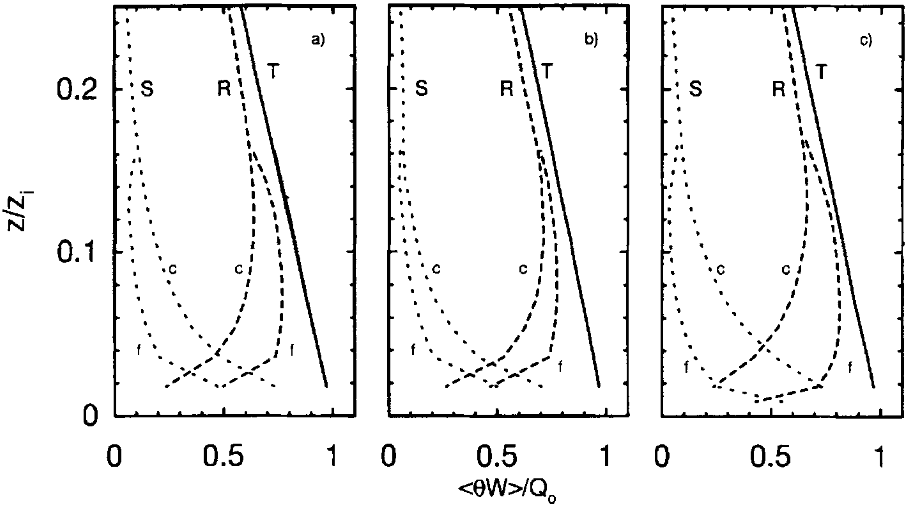

*Figure 6.* Heat flux profiles for cases; (a) $N2$ one-way nesting, fine grid $150^2 \times 10$, (b) $N3$ two-way nesting, fine grid $150^2 \times 10$, and (c) $N5$ two-way nesting, fine grid $250^2 \times 20$; in each total heat flux $\langle \bar{\theta}\bar{w} \rangle_{\text{total}}$ is solid line $T$, resolved heat flux $\langle \bar{\theta}\bar{w} \rangle_R$ dashed line $R$, and SGS heat flux $\langle \bar{\theta}\bar{w} \rangle_{\text{SGS}}$ is dotted line $S$; coarse and fine meshes are labeled $c$ and $f$.

shown nondimensionalised by $Q_0$. The total heat flux is observed to be a smooth function across the grid interface for both the one-way and two-way solutions for the grid resolutions considered. Here the effect of nesting is quite apparent in the separation between resolved and SGS heat fluxes. For instance, the vertical location where the resolved and SGS heat fluxes cross occurs at about $0.04z_i$ for case $N2$ in the coarse grid and at about $0.01z_i$ for the finest resolution considered (case $N5$). At a given height, say $z = 0.02z_i$, the resolved heat flux increases from about 25% to more than 75% of the total with increasing grid refinement. In the case of one-way interaction, the resolved and SGS fluxes in the fine grid are reasonably well behaved and roughly comparable to their counterparts in case $N3$ with two-way interaction. This might be expected since the fine mesh density in $N2$ and $N3$ are identical. Notice that for one-way computations, see Figure 6a, two solid lines are shown for the total heat flux in the surface layer which result from separate computations on the coarse and fine meshes. The average total heat flux in the fine grid is quite close to the value obtained on the coarse grid. In the cases with two-way interaction only one curve is shown for the total heat flux since by definition (see Section 3.5) the total flux on the coarse and fine grids are identical.

The ensemble statistics for the vertical momentum flux $\langle \bar{u}\bar{w} \rangle$ are next shown in Figure 7 for the same simulations as in Figure 6. Here the momentum flux is presented normalized by $u_*^2$. Similar trends are observed as for the heat flux, with the resolved momentum flux perhaps contributing an even bigger portion to the total flux as the grid spacing decreases. For case $N5$, the resolved momentum flux is more than 80% of the total flux down to about $z = 0.03z_i$. Again a smooth

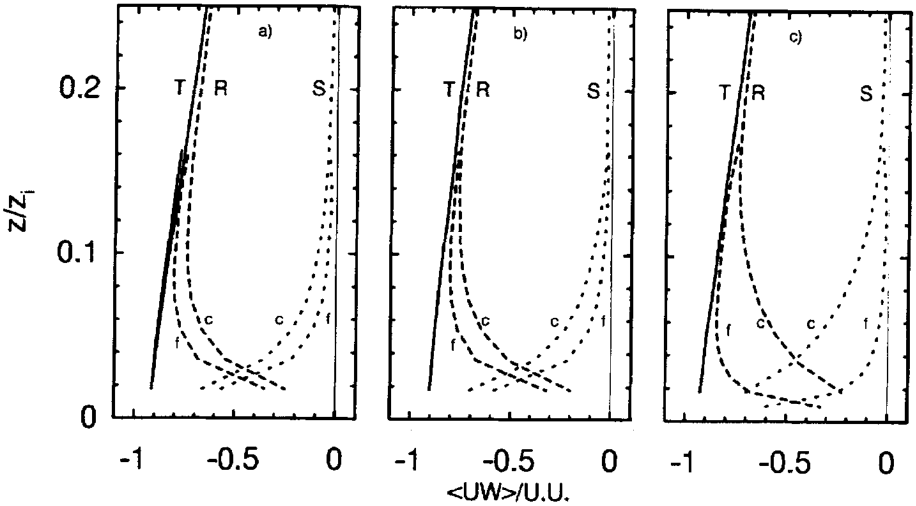

*Figure 7.* Same simulations as in Figure 6, but for vertical momentum flux $\langle \bar{u}\bar{w} \rangle$; $\langle \bar{u}\bar{w} \rangle_{\text{total}}$ is solid line $T$, resolved $\langle \bar{u}\bar{w} \rangle_R$ is dashed line $R$, and SGS $\langle \bar{u}\bar{w} \rangle_{\text{SGS}}$ is dotted line S; coarse and fine meshes are labeled $c$ and $f$.

variation in the fluxes occurs as the upper boundary of the nested grid is crossed. (Because of Coriolis effects $\langle \bar{v}\bar{w} \rangle \neq 0$ and hence $\langle -\bar{u}\bar{w} \rangle_{\text{total}}/u_*^2 \leq 1.0$ at the surface.) Again, the one-way results are roughly comparably to the results with two-way interaction for the same resolution.

In Figure 8, ensemble averages of the $x$, $y$ and $z$ variances $\langle \bar{u}^2 \rangle$, $\langle \bar{v}^2 \rangle$, and $\langle \bar{w}^2 \rangle$, respectively, normalized by $w_*^2$ are displayed for the various nested simulations. Several points are noteworthy in this figure. First, grid nesting is observed to have a pronounced effect on the magnitude of all the variances. For example, at $z = 0.03 z_i$ for case $N5$, the resolved variance $\langle \bar{u}^2 \rangle$ increases from about 1.7 to 2.4 a 40% increase as the grid spacing decreases from 30 × 30 × 9 m to 6 × 6 × 4.5 m. At the same $z$ location the $\bar{w}$ variance is increased by more than a factor of 3 in the fine grid. Also, two-way interaction has a favorable effect on the flow properties near the grid interface; with two-way interaction a smooth transition from the fine-to-coarse grid is observed for all three velocity variances. With one-way nesting, $\langle \bar{u}^2 \rangle$ and $\langle \bar{v}^2 \rangle$ display local maximums at the last $U$ grid point in the nested mesh, i.e., at grid node $M - 1/2$ in Figure 2. Moreover, this behaviour is not localised and appears to propagate downward through the surface-layer region. We found that the magnitude and exact position of this local maximum varied depending on the aspect ratio of the two meshes, i.e., the amount of refinement in the nested grid compared to the coarse grid, and also whether the upper boundary of the nested mesh was collocated at a $W$ or $U$ grid level. This behaviour associated with one-way interaction schemes reduces the allowable integration time step $\Delta t$ compared to cases with two-way interaction.

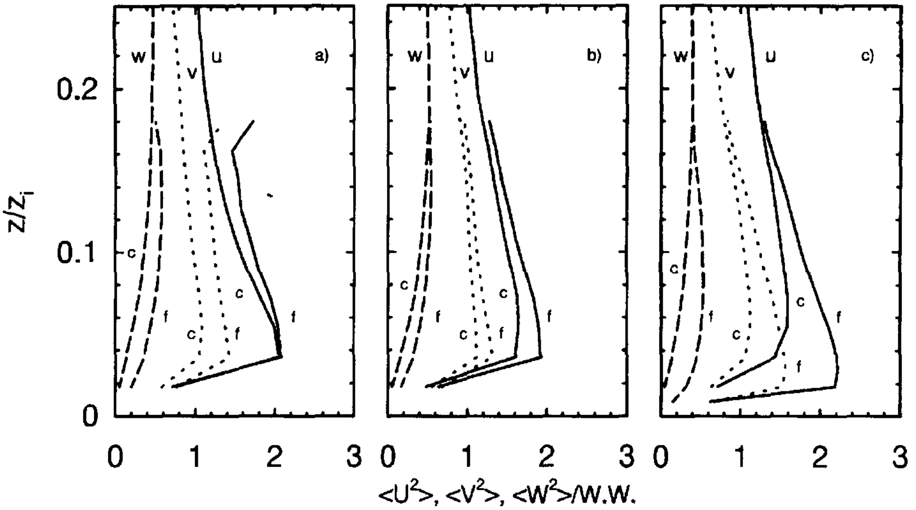

*Figure 8.* Same simulations as in Figure 6, but for velocity variances $\langle\bar{u}^2\rangle$ is solid line $u$, $\langle\bar{v}^2\rangle$ is dotted line $v$, and $\langle\bar{w}^2\rangle$ is dashed line $w$; coarse and fine meshes are labeled $c$ and $f$.

The root-mean-square (rms) resolved pressure $\langle\bar{\pi}^2\rangle^{1/2}$, normalized by $u_*^2$, shown in Figure 9 provides additional evidence for the non-physical behaviour observed near the grid interface with one-way interaction. The variation of the rms pressure suggests that turbulent motions are trapped in the nested mesh and are being reflected back into the domain at the upper boundary with one-way interaction. Meanwhile, with two-way interaction, the pressure and velocity are matched throughout the overlap region and thus the pressure displays a smooth transition across the grid interface.

All higher order resolved moments were found to increase with grid refinement. This is illustrated by the vertical velocity skewness $\langle\bar{w}^3\rangle/\langle\bar{w}^2\rangle^{3/2}$ depicted in Figure 10. The total skewness (resolved plus SGS) is not shown since the SGS contribution to the skewness is not available. As a result, we cannot state whether the total skewness remains the same for the fine and coarse simulations. Notice that on the fine grids this triple moment remains positive throughout the entire surface layer region. Previously in coarser LES, unrealistic negative values of the skewness were found (e.g., Schmidt and Schumann, 1989).

## 4.4. EFFECT OF SURFACE NESTING ON OUTER REGION

An important issue is the extent fine scale motions in the surface layer impact the PBL as a whole. For instance, if the global properties of the PBL are very sensitive to the details of the fine scale motions near the surface then the rational for performing LES is questionable. A means of gauging the importance of fine scale motion to the whole PBL is to compare ensemble statistics obtained from the

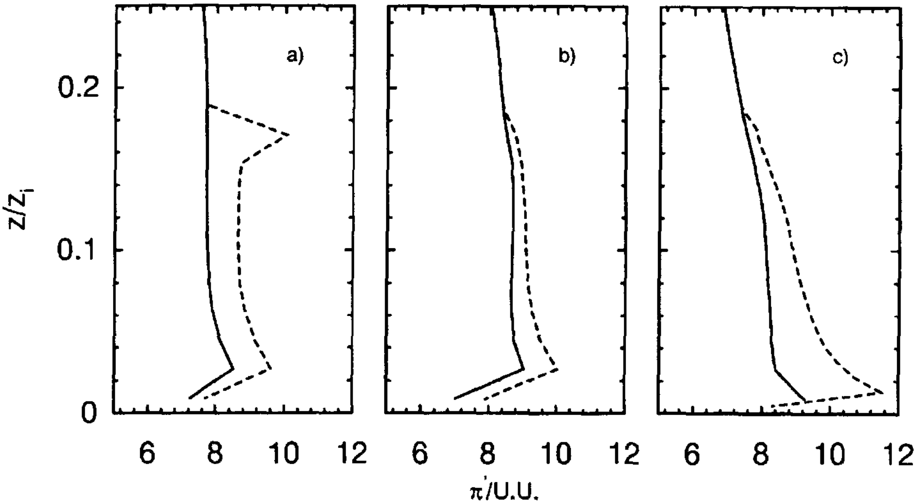

*Figure 9.* *rms* pressure $\langle \tilde{\pi}^2 \rangle^{1/2}$ for same simulations as in Figure 9; solid line coarse mesh and dashed line fine mesh.

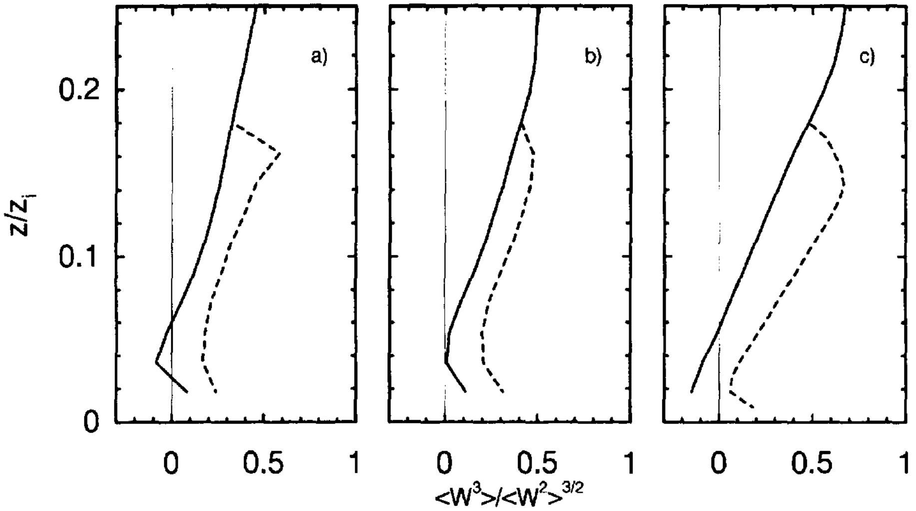

*Figure 10.* Vertical velocity skewness for same simulations as in Figure 6; solid line coarse mesh and dashed line fine mesh.

different simulations with and without surface-layer nesting. Comparison results are presented in Figures 11, 12, and 13 for the heat flux, vertical momentum flux $\langle \tilde{u}\tilde{w} \rangle$, and turbulent kinetic energy, respectively. In each figure, results from simulations $N1$, $N3$ and $N5$ are compared over the vertical extent $0 \leq z \leq 1.1 z_i$. It is important to point out that in the surface-layer region of the two-way nested calculations the resolved and SGS motions shown are the result of anterpolation of the fine mesh solutions, i.e., the fine mesh solutions are anterpolated to the coarse

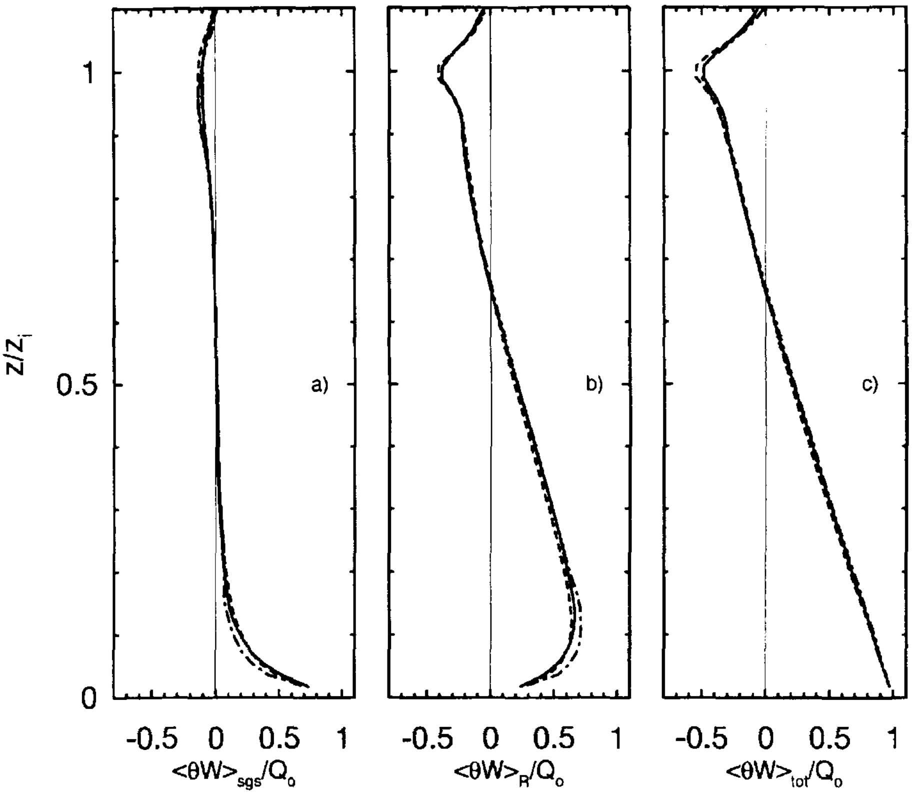

*Figure 11.* Ensemble averaged heat flux $\langle\bar{\theta}\bar{w}\rangle$ for; (a) SGS, (b) resolved, and (c) total; in each solid line $N5$, dashed-dotted line $N3$, and short dashes $N1$.

mesh resolution in the overlap region. Thus the results we present are for identical coarse mesh resolutions. The only changes in the resolved and SGS motions in the coarse grid come about as a consequence of the coupling with the fine scale motions in the surface-layer region, and statistical uncertainity associated with averaging.

The first impression from these results is that the total heat and momentum flux in the outer region of the PBL, i.e., $z \geq 0.2z_i$, are nearly independent of the surface layer resolution at least for the cases considered. $\langle\bar{\theta}\bar{w}\rangle_{\text{total}}$ and $\langle\bar{u}\bar{w}\rangle_{\text{total}}$ exhibit linear variations with height as expected for a quasi-steady state. The level of statistical uncertainity in computing the fluxes prevents clear trends from emerging as the surface resolution is increased. However, closer inspection of the results in the surface layer region suggests that the coarse mesh resolved fluxes contribute less to the total flux as the surface resolution is refined. At the same time, the SGS contribution exhibits an opposite trend with resolution in order to keep the total flux the same for the different cases. This trend is most visible in the results for the vertical momentum flux. For instance, at $z = 0.054z_i$, $\langle\bar{u}\bar{w}\rangle_R/u_*^2 = -0.56$

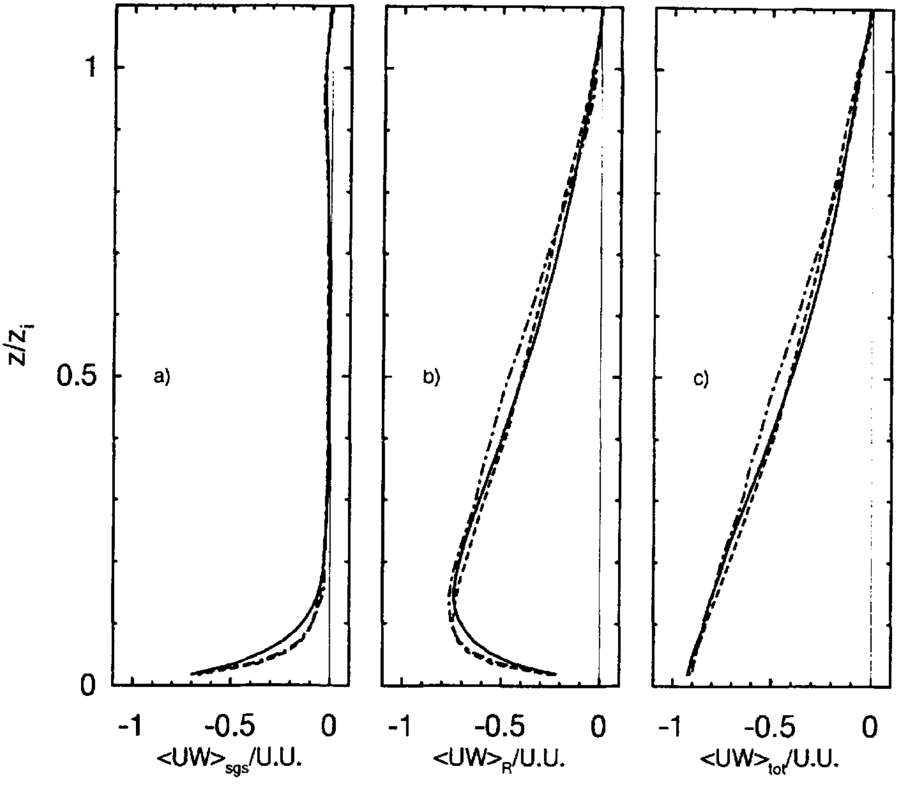

*Figure 12.* Ensemble averaged vertical momentum flux $\langle\bar{u}\bar{w}\rangle$ for same simulations as in Figure 11; (a) SGS, (b) resolved, and (c) total.

and $\langle\bar{u}\bar{w}\rangle_{\text{sgs}}/u_*^2 = -0.35$ in case $N5$ while at the same position for case $N2$ the momentum flux breakdown is $\langle\bar{u}\bar{w}\rangle_{\text{R}}/u_*^2 = -0.69$ and $\langle\bar{u}\bar{w}\rangle_{\text{sgs}}/u_*^2 = -0.22$.

The TKE normalised by $w_*^2$, seen in Figure 13, displays slightly more variation than the fluxes for the different simulations. For $z \geq 0.2z_i$, the SGS, resolved and total eddy energy are nearly independent of the surface layer resolution. Meanwhile in the surface layer, the resolved TKE appears to decrease as the surface layer resolution is refined, i.e., case $N5$ has less resolved TKE than case $N2$, similar to the trend observed for the momentum flux. Also in the surface layer, the SGS energy shows a clear increase as the resolution is refined. The net outcome of these trends is to keep the total TKE in the surface-layer region reasonably steady although the total eddy energy appears to increase slightly with increasing grid refinement. Overall from these results we conclude that the average global properties of this particular PBL are only slightly influenced by substantially increasing the grid resolution in the surface layer.

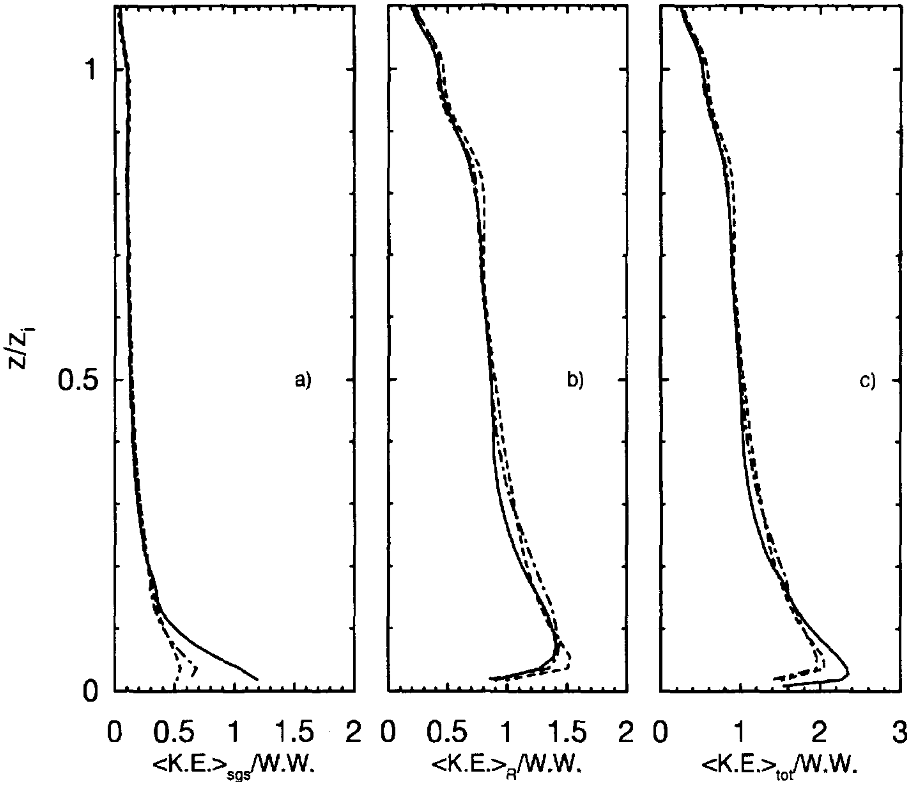

*Figure 13.* Ensemble averaged turbulent kinetic energy for same simulations as in Figure 11; (a) SGS, (b) resolved, and (c) total.

### 4.5. SCALE DISTRIBUTION OF EDDY ENERGY AND FLUXES

Grid nesting increases the resolved energy and flux motions in the surface layer which is a consequence of the length scale dependence in our SGS model (e.g., Moeng and Wyngaard, 1988). It is then important to investigate in greater detail the scale content of the increased resolved motions, i.e., in simulations with surface layer nesting (fine resolution) do the increases in resolved eddy variance and fluxes come only from scales $l \leq \Delta_c$ or from all turbulence scales.

One-dimensional longitudinal spectra of the $\tilde{u}$ and $\tilde{w}$ velocity components and potential temperature, i.e., $\phi_{uu}(\kappa_1)$, $\phi_{ww}(\kappa_1)$, and $\phi_{\theta\theta}(\kappa_1)$, where $\kappa_1$ is the wavenumber in the $x$ direction, were computed to discern the effect of mesh resolution on the energy content of the turbulence. These 1-D spectra were found by first computing 2-D Fourier transforms in a horizontal plane, then summing over all $y$-component wavenumbers $\kappa_2$, and finally averaging over multiple time steps.

Spectral estimates as functions of the dimensionless wavenumber $\kappa_1 z_i$ at several heights in the PBL are depicted in Figures 14 and 15 for simulations with and without surface layer nesting, $N5$ and $N1$, respectively. In Figure 14, the $\bar{u}$ and $\bar{\theta}$ spectra are displayed at $z/z_i = (0.027, 0.063, 0.099)$, and $\bar{w}$ spectra at $z/z_i = (0.036, 0.072, 0.108)$. In the outer region, Figure 15, $\bar{u}$ and $\bar{\theta}$ spectra are displayed at $z/z_i = (0.207, 0.495, 0.837)$ and at $z/z_i = (0.216, 0.504, 0.846)$ for $\bar{w}$ spectra. Note that all spectra are multiplied by the wavenumber $\kappa_1$, to emphasise the small scale motions, and are normalised, as appropriate, by $u_*^2$ and $\theta_*^2$. In the surface layer, inspection of these spectra reveals that the influence of fine surface layer resolution is not localised to high wavenumbers (small scales) but alters the energy across all wavenumbers. For the $\bar{u}$ and $\bar{\theta}$ spectra, the energy at wavenumbers $\kappa_1 z_i \geq 12$ is greatly increased as the mesh resolution becomes finer. Also, the $\bar{u}$ and $\bar{\theta}$ spectra obtained with grid nesting, all have broader and lower peaks than their no-nesting counterparts. The most dramatic change is, however, observed in the $\bar{w}$ spectra, where the fine mesh resolution results display a shift in both magnitude and location of the peak energy. For example, in the no-nesting case the peak energy in the $\bar{w}$ spectra occurs at $\kappa_1 z_i = 10$ but peaks at $\kappa_1 z_i = 30$ in the case with nesting; at $z/z_i = 0.036$ the spectral peak is increased by more than a factor of 3 as the resolution becomes finer. It should be noted that the analysis of Peltier *et al.* (1995) also suggests that the $\bar{w}$ field is more sensitive to grid resolution than the other velocity components.

Outside of the nested region, seen in Figure 15, the $\bar{u}$ and $\bar{\theta}$ spectra with and without surface-layer nesting are quite similar despite the statistical uncertainty associated with the averaging. The intermittency of the $\bar{\theta}$ signal makes estimation of the small wavenumbers (large scales) difficult. Here, the $\bar{w}$ specta show more influence of surface nesting extending out to perhaps $z/z_i \geq 0.22$; recall that the upper boundary of the nested grid is located at $z/z_i = 0.18$. Near the capping inversion ($z/z_i = 0.84$) the spectra for all three variables with and without surface layer nesting are nearly identical.

The spectral results provide evidence that grid nesting intensifies the eddy motions at high wavenumbers and shifts the peak energy scale in the $\bar{w}$ spectrum to smaller scales. These same trends are also visible in instantaneous contour plots of $\bar{u}$, $\bar{w}$, and $\bar{\theta}$, pictured in Figure 16. In this figure, the left hand panels are results from no-nesting simulation $N1$ and the right hand panels the fine-mesh nesting simulation $N5$; for a particular variable the same contour levels are used across the simulations. These typical cross sectional $x - y$ snapshots of the flow field are taken at $z/z_i = 0.072$ within the nested region. Examination of the fields reveals considerable more small-scale activity in the fine mesh simulation; especially noticeable is the decrease in dominant scale in the $\bar{w}$ field. Similar findings were also observed in a study of Langmuir turbulence in the ocean (McWilliams *et al.*, 1996). Also, noticeable in Figure 16 is an apparent shift in orientation of the dominant structure (like convective rolls) in the $\bar{u}$ and $\bar{\theta}$ fields. Previously, Moeng and Sullivan (1994) found that for a comparable simulation, using $96^3$ gridpoints the dominant roll structure was oriented west–east. In the current no-nesting simulation this structure appears to be roughly oriented from southwest–northwest, and we

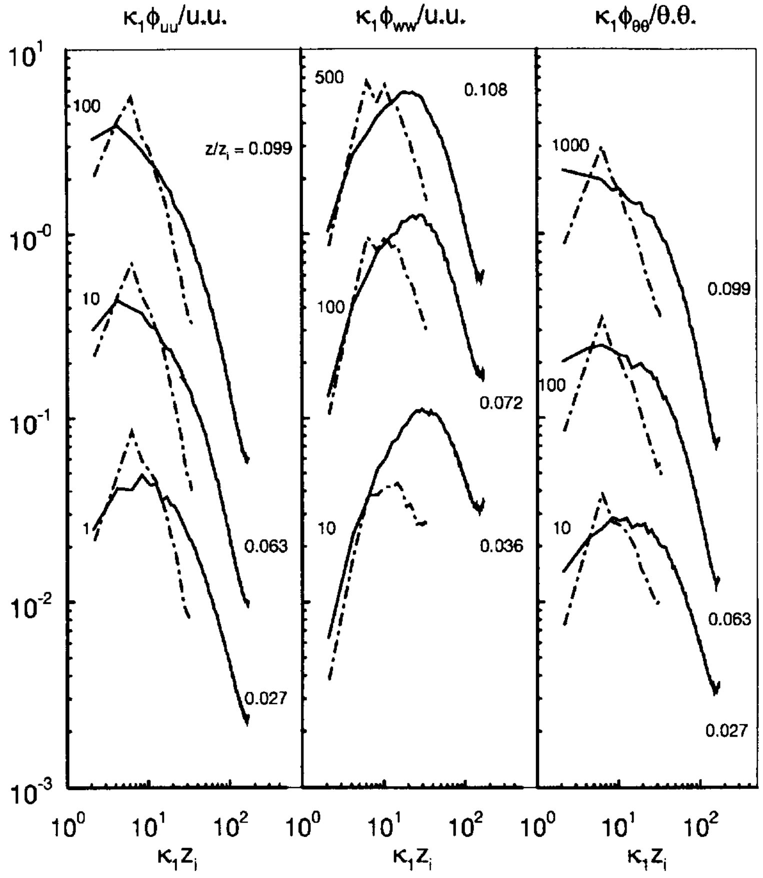

*Figure 14.* Longitudinal spectra of velocity components $\bar{u}$ and $\bar{w}$ and potential temperature $\bar{\theta}$ in the surface layer. Spectra of $\bar{u}$ and $\bar{\theta}$ are at $z/z_i = (0.027, 0.063, 0.099)$, and $\bar{w}$ spectra at $z/z_i = (0.036, 0.072, 0.108)$. All spectra are multiplied by wavenumber $\kappa_1$ and normalized by either $u_*^2$ or $\theta_*^2$; solid line fine mesh simulation $N5$ and dashed-dotted line coarse mesh simulation $N1$. The data are scaled by the factors on the left of each plot to avoid overlap.

speculate that the spectral peaks in the coarse resolution simulation in Figure 14 are associated with this structure. Apparently grid refinement serves to realign the structure roughly west-east as seen in the fine mesh $\bar{u}$ and $\bar{\theta}$ fields. At the same time, the spatial organization of these large roll structures appears to be weakened by small-scale resolved motions. In the outer region, the $\bar{u}$, $\bar{w}$ and $\bar{\theta}$ fields are comparable in appearance (results not shown). This illustrates that for this particluar flow the effects of nesting are localised and do not propagate substantially to the outer region.

$\bar{w}$ is most influenced by the enhanced grid resolution in the surface layer, and thus has important consequences for the vertical eddy fluxes. Cospectra of the vertical momentum flux $\phi_{uw}(\kappa_1)$ and heat flux $\phi_{\theta\omega}(\kappa_1)$ are displayed in Figures 17 and 18 using log-linear coordinates at several different heights; the cospectra

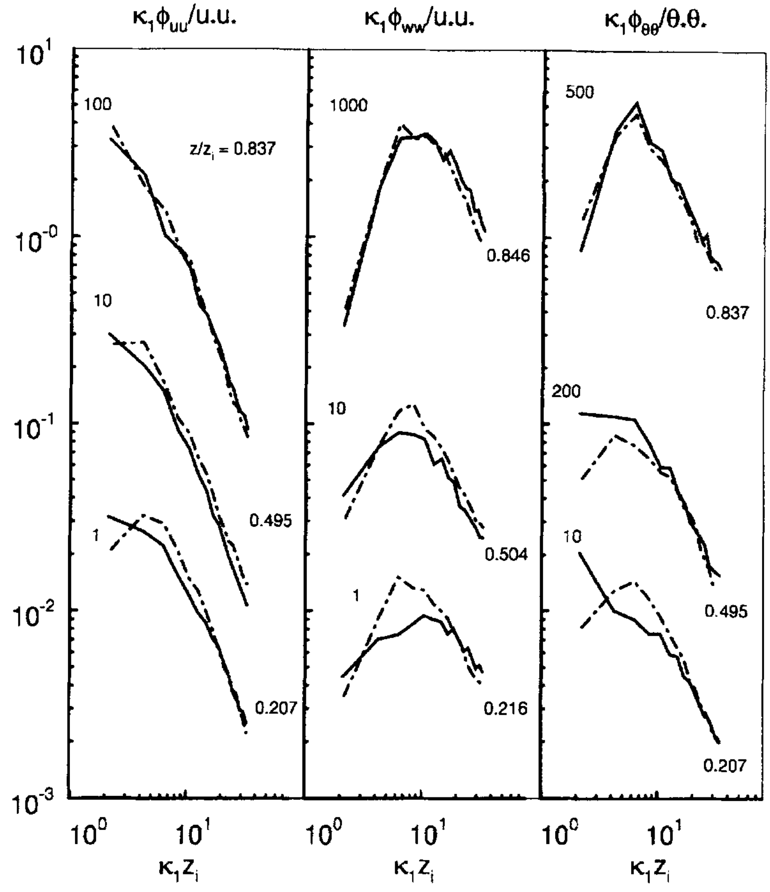

*Figure 15.* Longitudinal spectra of velocity components $\bar{u}$ and $\bar{w}$ and potential temperature $\bar{\theta}$ for the same simulations as in Figure 14. Spectra of $\bar{u}$ and $\bar{\theta}$ are at $z/z_i = (0.207, 0.495, 0.837)$ and at $z/z_i = (0.216, 0.504, 0.846)$ for $\bar{w}$ spectra.

are normalized by $u_*^2$ and $Q_0$ appropriately and multiplied by $\kappa_1$. Once again with grid nesting the spectral peak in the fluxes shifts to higher wavenumbers primarily as a consequence of the energy-scale content of $\bar{w}$. At wavenumbers $\kappa_1 z_i \geq 15$ the cospectra of the fine mesh fluxes are of considerably greater amplitude compared to the no-nesting simulation.

## 4.6. IMPLICATIONS OF GRID NESTING FOR COHERENT STRUCTURES

Much evidence, both experimental and numerical, has been accumulated that turbulent flows at sufficiently large Reynolds or Rayleigh numbers are highly intermittent, under both buoyant and shear dominated conditions. These intermittent processes are generally believed to be associated with what are loosely termed "coherent structures"; these are recurrent, spatially local flow patterns which are

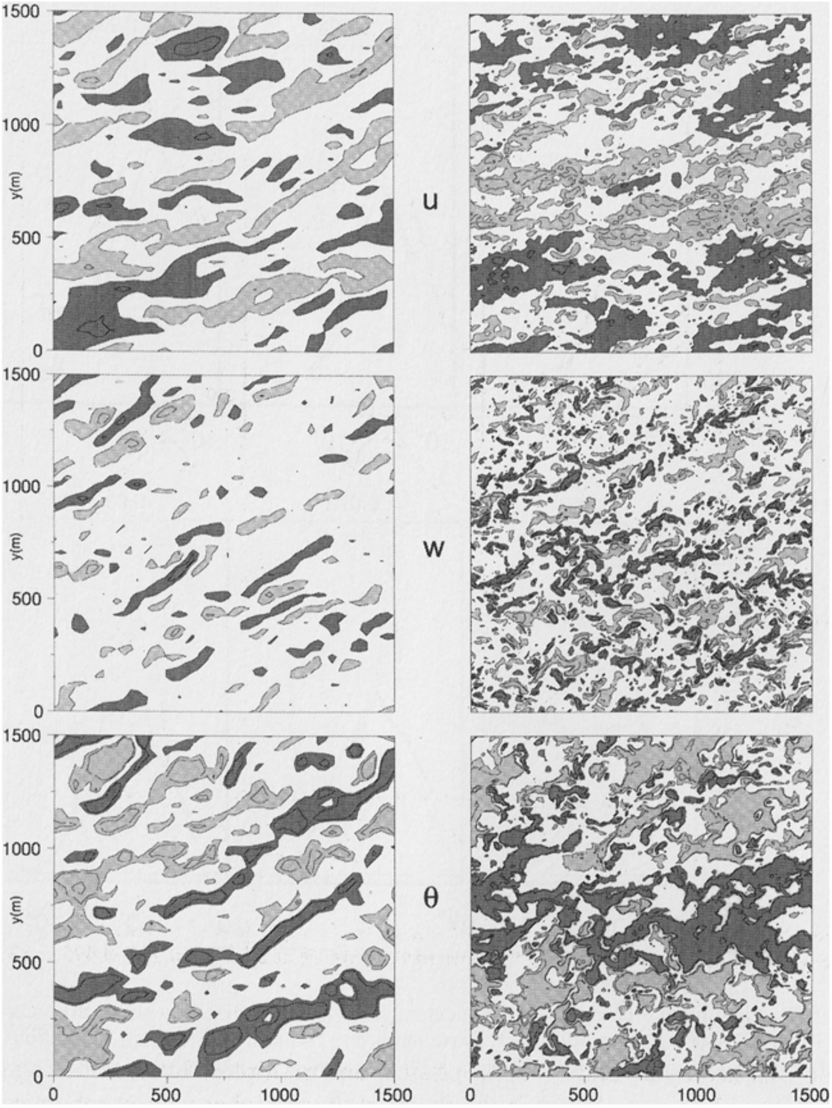

*Figure 16.* Velocity and potential temperature contours at $z/z_i = 0.072$ from coarse mesh $N1$ (left panels) and fine mesh $N5$ (right panels). $\bar{u}$ contours $(-2.0, -0.75, 0.75, 2.0)$ with light (dark) shading for values below (above) $-0.75$ $(0.75)$, $\bar{w}$ contours $(-1.0, -0.50, 0.50, 1.0)$ shading $-0.50$ $(0.50)$, $\bar{\theta}$ contours $(-0.09, -0.06, 0.06, 0.09)$ shading $-0.06$ $(0.06)$.

long lived in a Lagrangrian reference frame (i.e., moving with the local fluid velocity).

Further, it is also believed that coherent structures are the agents responsible for the production and maintenance of strong flux fields in the PBL (e.g., McWilliams *et al.*, 1996; Gerz *et al.*, 1993; Mahrt and Gibson, 1992; and Schmidt and Schumann,

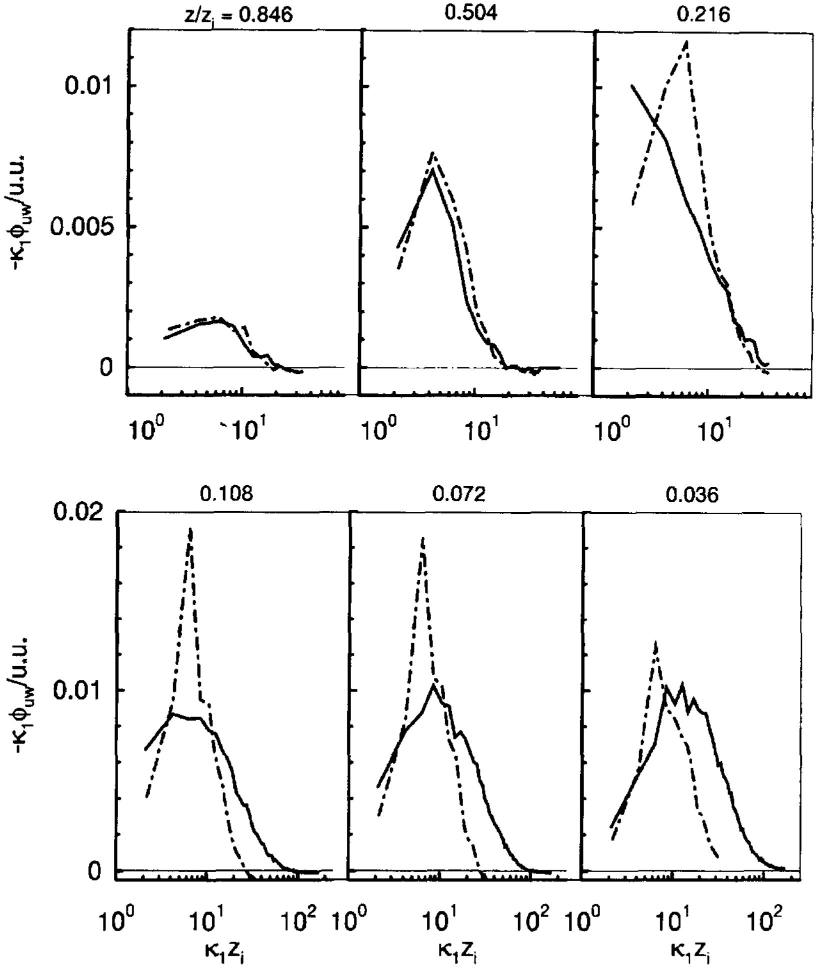

*Figure 17.* Longitudinal cospectra of momentum flux $\overline{uw}$ normalized by $u_*^2$ at different heights in the PBL. All spectra are multiplied by wavenumber $\kappa_1$; solid line fine mesh simulation $N5$ and dashed-dotted line coarse mesh simulation $N1$. Note expanded horizontal scale in outer region.

1989). The present LES results suggest that as the surface-layer grid resolution is refined the resolved vertical velocity and flux fields are intensified, are more intermittent, and the dominant scale becomes smaller. Hence we are led to speculate that the scale and properties of the coherent structures have also changed, i.e., the structures are of smaller scale and are more intense. Future studies will explore the relationship between coherent structures and fluxes in the surface layer of the PBL using LES and grid nesting.

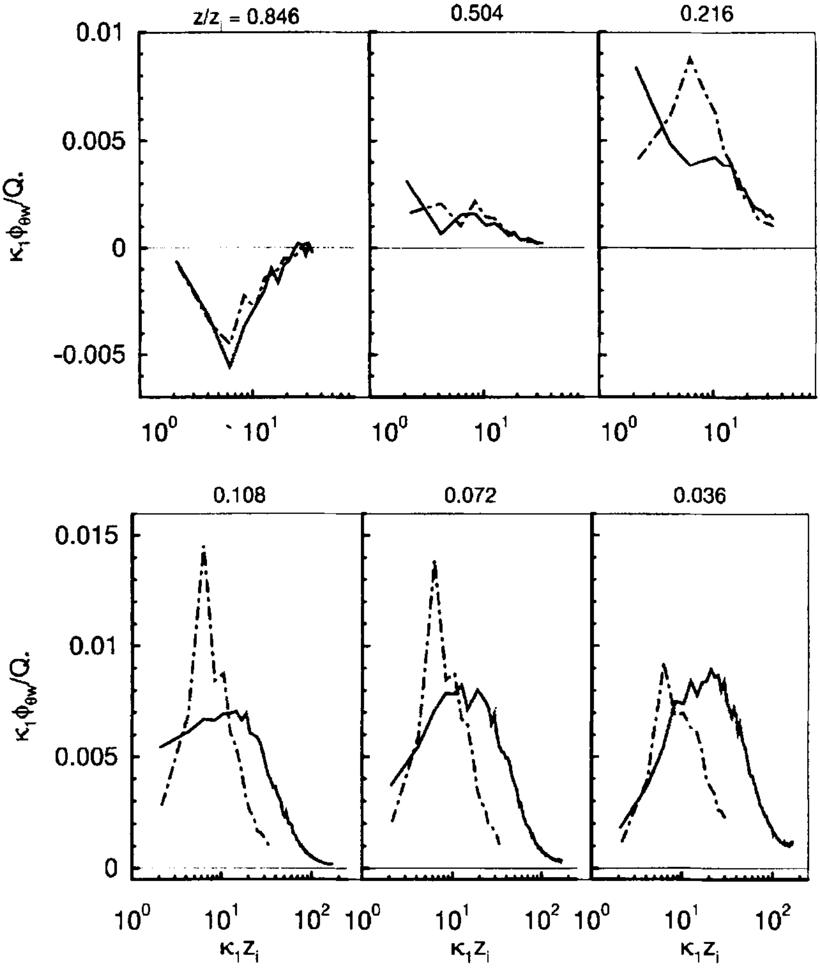

*Figure 18.* Longitudinal cospectra of heat flux $\overline{\theta w}$ normalized by $Q_0$ at different heights in the PBL. All spectra are multiplied by wavenumber $\kappa_1$; solid line fine mesh simulation $N5$ and dashed-dotted line coarse mesh simulation $N1$. Note expanded horizontal scale in outer region.

## 5. Summary and Conclusions

Large-eddy simulation (LES), with fixed grid resolution becomes less reliable near bounding surfaces because of the increasing importance of the sub-grid scale (SGS) motions compared to the resolved motions. In order to increase the resolved motions, and at the same time decrease the SGS motions, a grid nesting procedure, based on overlapping meshes, was implemented into our LES code. Inter-grid communication allows the coarse mesh solution to impose boundary conditions on the fine mesh (one-way interaction), and furthermore permits feedback from the fine mesh to the coarse mesh (two-way interaction). The two-way interaction scheme matches the velocity, pressure and potential temperature fields in the overlap region.

In the overlap region, the SGS motions on the coarse grid can be expressed in terms of fine mesh resolved and SGS motions through Germano's identity (Germano *et al.*, 1991) used to develop dynamic SGS models. Our procedure for diagnosing the SGS motions in the coarse grid in the overlap region conserves the total flux from the fine grid and thus differs from other nesting schemes which compute the SGS motions in the coarse grid using approximate rules.

Qualitative and quantitative measures are used to study the effects of one-way and two-way grid nesting. Instantaneous flow visualisation provides an overall impression of the changes in flow structure brought about by nesting while these effects are quantified by comparing ensemble statistics (variances, fluxes and spectra). Because of the stochastic nature of turbulence we have no exact benchmark flow field for comparison, but expect that our solutions with high resolution (smaller SGS motions) are a more faithful representation of high Reynolds number turbulent flows than simulations with coarser resolution.

Simulations of a slightly convective, strong shear planetary boundary layer (PBL) were carried out with varying surface-layer resolutions. Grid refinements in the surface layer up to (5, 5, 2) times finer in the $(x,\ y,\ z)$ directions were investigated. Two-way interaction solutions on the coarse and fine meshes are successfully matched in the overlap region on an instantaneous basis, and the turbulent motions on the fine grid blend smoothly into the coarse grid across the grid interface. In the surface layer, the resolved heat flux on the finest nested mesh is increased by more than a factor of 3 compared to its value on the coarse mesh. Similar increases in the resolved vertical momentum flux $\langle \bar{u}\bar{w} \rangle$ and turbulent kinetic energy (TKE) are also found.

Simulations with one-way interaction suggest that the fine mesh fields, despite being driven by coarse mesh boundary conditions, differ considerably from their coarse mesh counterparts on an instantaneous point-by-point basis. A spurious maximum was found in the $\bar{u}$ and $\bar{v}$ velocity variances just below the nested grid interface.

Velocity and temperature spectra illustrate that the effect of surface-layer grid nesting is not confined to high wavenumbers, but spills over into the small wavenumbers (large scales). Most significantly the spectra of the vertical velocity $\bar{w}$ show that the magnitude of the peak energy is increased by a factor of 3 very near the surface and the peak energy scale shifts towards higher wavenumbers. This shift in scale and intensification of eddy fluctuations is also visible in a comparison of instantaneous flow fields between nesting and no-nesting simulations. Cospectra of the vertical momentum and heat fluxes also display a similar shift in scale content with fine surface-layer resolution.

In the mixed layer of the PBL, the average heat and momentum fluxes as well as the spectra of velocity and temperature are nearly identical with and without surface-layer nesting. This suggests that the effects of the small scales in the surface layer do not propagate very far upward into the PBL.

From these results we conclude that fine resolution is required to resolve the details of the turbulent motions in the surface layer. Typical modest resolution LES in the surface layer underpredicts the magnitude and scale content of the vertical velocity fluctuation and thereby masks the dominant flux-carrying structures. At the same time, however, increased resolution in the surface layer does not appreciably alter the ensemble statistics of the resolved and SGS motions outside of the nested region.

## Acknowledgements

We thank Keith Ayotte, Terry Clark, Bill Hall, Ching-Long Lin, and Joe Werne for their useful discussions. This work was supported by the Office of Naval Research and Minerals Management Service through contract N00014-92-F-0117 and by the National Science Foundation through the National Center for Atmospheric Research.

## Appendix A. Interpolation and Anterpolation Rules

In any $x-y$ plane, trigonometric polynomials (or Fourier series) are used to perform all interpolations and anterpolations. For instance, any coarse mesh variable $\Phi$ discretized at $N$ coarse mesh grid nodes

$$X_j = \frac{2\pi j}{N} \quad j = 0, \ldots, N-1, \tag{A1}$$

can be represented by

$$\Phi(X_j) = \sum_{k=-N/2}^{N/2-1} \hat{\Phi}_k e^{ikX_j} \quad j = 0, \ldots, N-1, \tag{A2}$$

where the coarse mesh discrete coefficients $\hat{\Phi}_k$ are

$$\hat{\Phi}_k = \frac{1}{N} \sum_{j=0}^{N-1} \Phi(X_j) e^{-ikX_j} \quad -N/2 \leq k \leq N/2-1, \tag{A3}$$

and $k$ are dimensionless wavenumbers. A fine mesh variable $\phi$ results from applying the coarse-to-fine interpolation rule

$$\phi(x_l) = \sum_{k=-M/2}^{M/2-1} \hat{\phi}_k e^{ikx_l} \quad l = 0, \ldots, M-1, \tag{A4}$$

at the $M$ fine mesh nodes

$$x_l = \frac{2\pi l}{M} \quad l = 0, \ldots, M-1, \tag{A5}$$

where the fine mesh discrete coefficients $\hat{\phi}_k$ written in terms of coarse mesh coefficients $\hat{\Phi}_k$ are

$$\begin{aligned} \hat{\phi}_k &= \hat{\Phi}_k && -N/2+1 \le k \le N/2-1 \\ \hat{\phi}_k &= \frac{\hat{\Phi}_k}{2} && k = \pm N/2 \\ \hat{\phi}_k &= 0 && -M/2 \le k \le -N/2 \\ \hat{\phi}_k &= 0 && N/2 < k \le M/2-1. \end{aligned} \tag{A6}$$

Note that the fine mesh coefficients are set equal to their coarse mesh counterparts where available, otherwise they are simply set equal to zero.

In a similar fashion, fine-to-coarse mesh anterpolations involve three steps. First, fine mesh data is transformed into Fourier space, then the fine mesh Fourier series is truncated and finally an inverse transform yields coarse mesh data in physical space. Given fine mesh discrete coefficients $\hat{\phi}_k$ at wavenumbers $M/2 \le k \le M/2 - 1$ the coarse mesh coefficients are

$$\begin{aligned} \hat{\Phi}_k &= \hat{\phi}_k && -N/2+1 \le k \le N/2-1 \\ \hat{\Phi}_k &= 2\hat{\phi}_k && k = -N/2. \end{aligned} \tag{A7}$$

Identical steps are followed in performing interpolations and anterpolations in the $y$ direction. In physical space these coarse-to-fine interpolations and fine-to-coarse anterpolations yield identical results at all common grid nodes $X_j = x_l$, and furthermore are reversible. The proposed anterpolation rule is equivalent to applying a sharp cutoff filter to the fine mesh variables at the smallest scale of the coarse grid. Fast Fourier Transforms (FFTs) are used to sum the series in the above expressions.

The use of finite differences in the vertical direction requires special treatment in the anterpolation operator. For resolved and SGS variables which are needed at $W$ grid levels (vertical velocity $\bar{w}$ and SGS energy $e$) only the horizontal spectral interpolation and anterpolation described above is applied. On the other hand, for variables required at $U$ grid levels (horizontal velocities $\bar{u}$ and $\bar{v}$) some form of anterpolation in the vertical direction is required. A vertical integral of fine mesh data between two coarse $W$ levels is performed

$$\Phi(z_{K-1/2}) = \frac{1}{\Delta z_c} \int_{z_{M-2}}^{z_M} \phi(z)\, \mathrm{d}z, \tag{A8}$$

where $\Delta z_c = z_M - z_{M-2}$ in Figure 2. This integral is discretised using a midpoint rule. Application of (A8) to resolved fine mesh data ($\overline{u}$ and $\overline{v}$) satisfies the coarse mesh incompressibility condition.

## References

Andrén, A., Brown, A. R., Graf, J., Mason, P. J., Moeng, C.-H., Nieuwstadt, F. T. M., and Schumann, U.: 1994, 'Large-Eddy Simulation of a Neutrally Stratified Boundary Layer: A Comparison of Four Computer Codes', *Quart. J. R. Meteorol. Soc.* **120**, 1457–1484.

Clark, T. L. and Farley, R. D.: 1984, 'Severe Downslope Windstorm Calculations in Two and Three Spatial Dimensions Using Anelastic Interactive Grid Nesting: A Possible Mechanism for Gustiness', *J. Atmos. Sci.* **41**, 329–350.

Clark, T. L. and Hall, W. D.: 1991, 'Multi-Domain Simulations of the Time Dependent Navier–Stokes Equations: Benchmark Error Analysis of Some Nesting Procedures', *J. Comp. Phys.* **92**, 456–481.

Danabasoglu, G., Biringen, S., and Street, C. L.: 1994, 'Application of the Spectral Multidomain Main Method to the Navier–Stokes Equations', *J. Comp. Phys.* **113**, 155–164.

Deardorff, J. W.: 1980, 'Stratocumulus-Capped Mixed Layers Derived from a Three-Dimensional Model', *Boundary-Layer Meteorol.* **18**, 495–527.

Germano, M., Piomelli, U., Moin, P., and Cabot, W. H.: 1991, 'A Dynamic Subgrid-Scale Eddy Viscosity Model', *Phys. Fluids A.* **3**, 1760–1765.

Gerz, T., Howell, J., and Mahrt, L.: 1994, 'Vortex Structures and Microfronts', *Phys. Fluids* **3**, 1242–1251.

Grell, G. A., Dudhia, J., and Stauffer, D. R.: 1994, 'A Description of the Fifth-Generation Penn State/NCAR Mesoscale Model (MM5)', NCAR technical note, NCAR/TN-398 + STR.

Henderson, R. and Karniadakis, G. E.: 1991, 'Hybrid Spectral-Element-Low-Order Methods for Incompressible Flows', *J. Sci. Comp.* **6**, 79–100.

Klemp, J. and Duran, D.: 1983, 'An Upper Boundary Condition Permitting Internal Gravity Wave Radiation in Numerical Mesoscale Models', *Mon. Wea. Rev.* **11**, 430–444.

Mahrt, L. and Gibson, W.: 1992, 'Flux Decomposition into Coherent Structures', *Boundary-Layer Meteorol.* **40**, 283.

McWilliams, J. C., Gallacher, P. C., Moeng, C.-H., and Wyngaard, J. C.: 1993, 'Modeling the Oceanic Planetary Boundary Layer', *Large-Eddy Simulations of Turbulent Flows*, Lecture Notes in Engineering, Cambridge University Press, pp. 441–454.

McWilliams, J. C., Sullivan, P. P., and Moeng, C.-H.: 1996, 'Langmuir Turbulence in the Ocean', *J. Fluid Mech.*, In Press.

Moeng, C.-H.: 1984, 'A Large-Eddy-Simulation Model for the Study of Planetary Boundary-Layer Turbulence', *J. Atmos. Sci.* **41**, 2052–2062.

Moeng, C.-H., and Wyngaard, J. C.: 1988, 'Spectral Analysis of Large-Eddy Simulations of the Convective Boundary Layer', *J. Atmos. Sci.* **45**, 3575–3587.

Moeng, C.-H., and Sullivan, P. P.: 1994, 'A Comparison of Shear Buoyancy Driven Planetary-Boundary Flows', *J. Atmos. Sci.* **51**, 999–1022.

Nieuwstadt, F. T. M., Mason, P. J., Moeng, C.-H.: and Schumann, U.: 1991, 'Large-Eddy Simulation of the Convective Boundary Layer: A Comparison of Four Computer Codes', *8th Symposium on Turbulent Shear Flows*, Springer-Verlag.

Peltier, L. J., Wyngaard, J. C., Khanna, S., and Brasseur, J.: 1995, 'Spectra in the Surface Layer', *J. Atmos. Sci.*, In Press.

Perng, C. Y. and Street, R. L.: 1991, 'A Coupled Multigrid-Domain Splitting Technique for Simulating Incompressible Flows in Geometrically Complex Domains', *Inter. J. Numer. Methods in Fluids* **13**, 269–286.

Phillips, N. A. and Shukla, J.: 1973, 'On the Strategy of Combining Coarse and Fine Grid Meshes in Numerical Weather Prediction', *J. Appl. Meteorol.* **12**, 763–770.

Reynolds, W. C.: 1989, 'The Potential and Limitations of Direct and Large Eddy Simulations', *Whither Turbulence ? or Turbulence at the Crossroads*, Cornell University.

Skamarock, W. C. and Klemp, J. B.: 1993, 'Adaptive Grid Refinement for Two-Dimensional and Three-Dimensional Nonhydrostatic Atmospheric Flow', *Mon. Wea. Rev.* **121**, 768–804.

Spalart, P. R., Moser, R. D., and Rogers, M. M.: 1991, 'Spectral Methods for the Navier–Stokes Equations with One Infinite and Two Periodic Directions', *J. Comp. Phys.* **96**, 297.

Sullivan, P. P., McWilliams, J. C., and Moeng, C.-H.: 1994, 'A Subgrid-Scale Model for Large-Eddy Simulation of Planetary Boundary-Layer Flows', *Boundary-Layer Meteorol.* **71**, 247–276.

Walko, R. L., Tremback, C. J., Pielke, R. A., and Cotton, W. R.: 1995, 'An Interactive Nesting Algorithm for Stretched Grids and Variable Nesting Ratios', *J. Appl. Meteorol.* **34**, 994–999.
Wyngaard, J. C., 1984, 'Large-Eddy Simulation: Guidelines for its Application to Planetary Boundary Layer Research', US Army Research Office Contract No. 0804.